Seismic analysis of fluid mud

Detection of shear paramters in fluid mud and the relation between seismic velocities and yield stresses

Master of Science Thesis

for the degree of Master of Science in Applied Geophysics
by

Menno Buisman

TU Delft

Port of Rotterdam

IDEA LEAGUE
JOINT MASTER'S IN APPLIED GEOPHYSICS

Delft University of Technology, The Netherlands
ETH Zürich, Switzerland
RWTH Aachen, Germany

Dated: *August 8, 2019*

Supervisor(s):

Dr. Ir. Deyan Draganov

Dr. A Kirichek, Deltares

Committee Members:

Dr. ir. D.S. Draganov, TU Delft

Dr. A Kirichek, Deltares

Prof. Dr. H. Maurer, ETH Zurich

Abstract

In this research, a new measuring method to detect shear parameters in fluid mud is proposed, namely using shear waves, or S-waves opposed to the conventional pressure waves, or P-waves.
Currently, detecting fluid mud is done by the use of P-waves. This paper shows that conventional P-waves velocity measurements are unsuitable for linking velocities to the yield stress, which is likely caused due to gas in the mud. Opposed to this, S-wave velocities do show an logarithmic increase, which most likely can be linked to the yield stress development of fluid mud. Both S-wave velocities and yield-point measurements show an exponential increase over time and, because of this, it could be that there is a linear relation between them.
The difference why S-waves are more suitable for shear-strength measuring is due to their nature of propagation. S-waves do not propagate through gas and are therefore hardly effected by gas production, opposed to P-waves.
For this research, both P-and S-wave velocities are estimated from a transmission seismic experiment. Also, a frequency analysis has been conducted showing large similarities over time and for dissimilarities between different mud samples. The yield-point measurements are derived from a rheometer with the same mud sample used for the seismic experiments.
Besides a velocity analysis from the transmission measurements, also a reflection measurement has been conducted. The aim for this is to detect converted P-to S-waves and to detect the Scholte wave.
Furthermore, a dispersion analysis has been conducted, which is likely important since the relative change in S-wave velocities is small and the velocities are frequency-dependent.

Preface

This research is mend to further improve exciting methods and help establish new methods for monitoring fluid mud for the Port of Rotterdam. The Port of Rotterdam is expanding, making monitoring and dredging campaigns more important. There is need for improving the current techniques which allow for a better understanding of how which builds up in volune and strength in the harbor and river channels. This knowledge is needed because it could potentially allow vessels to safely navigate through fluid mud layers, resulting in a decrease for the need to dredge. Besides that this would reduce the maintenance costs, it would also reduce CO2 emissions, reduce noise and reduce the traffic on the channels.
This research was made possible with the help of a strong support group. First of all Dr. Deyan Draganov and Dr. Alex Kirichek who came with the idea to use different methods for monitoring campaigns and supported me along my research. Secondly Aukje Veltmeijer for helping me out whenever needed throughout my research process, with both sampling and coding, and finally Dr. Xu Ma for helping me with the lab measurements and Seismic Unix.

Menno Buisman
Delft, August 2019

Contents

List of Figures

1

Introduction

This chapter is intended as an introduction to my thesis for the Port of Rotterdam. It is a general introduction of the topic of monitoring fluid mud and the dredging criterion in the Port of Rotterdam. Also the research questions will be posed in this chapter.

1.1. Current and potential new dredging criterion

The Port of Rotterdam (PoR) is Europe's busiest port (Kiprop, 2018) and therefore it is of utmost importance to ensure safe passage for large vessels by the port's authorities. To allow for safe passage, fluid-like sediments, which will now be referred to as fluid mud, deposited by the rivers and tides must be dredged. Fluid mud is characterized by its low density and low shear strength. To ensure the nautical depth is maintained, the fluid mud is dredged once it reaches a density of 1.2 kg/l (McAnally et al., 2007).
Maintaining a fixed nautical depth requires intense dredging which leads to high costs. Currently, the criterion for dredging is only related to density of the fluid mud. Fontein and Van der Wal (2006) and Kirichek et al. (2018), proposed to restrict the maximum draft of the incoming vessels exerted by the vessel on the fluid mud, instead of looking at the density of the fluid mud. In other terms, the new criterion would be the yield point of the fluid mud, instead of the density.
In order to adopt this new criterion, in-situ rheological properties, such as shear strength and viscosity, of the fluid-mud need to be accurately determined. If this is possible, adopting the new criterion could potentially lead to less-frequent dredging, which would lead in return to a reduction of maintenance costs of the river channels.

The PoR currently tests various techniques to determine the rheological properties of the fluid mud. Some of the point measurement tools can be seen in Figure 1.1. These point measurement tools are very ineffective considering the size of the PoR. What also makes these point measurements ineffective is that the rheology parameters of the fluid mud can differ per river channel. For a more efficient way of measuring the fluid mud/ water interface and the fluid mud density, the PoR also uses acoustics in the form of echosounder. These echosounders measure at zero offset, implying only one receiver, and require point measurements to be calibrated with in order to derive the density. These point measures are required to create a synthetic density profile. This synthetic density is then compared to the measured density profile for validation.
To accurately determine the water/fluid mud interface is not a trivial task as shown by Schrottke (2006). Furthermore, while retrieving a sample for a point measurement, the sample gets disturbed and its rheological parameters get altered. Due to this, the accuracy of these measurements is limited. Besides, the echo sounders only relay on P-waves, giving only very little information about shear parameters.
To adopt a new criterion for dreding, the shear parameters need to be determined which is currently impossible with the echo sounders. However, it is likely that the shear parameters

Figure 1.1: Examples of rheology-based methods. From left to right: lab rheometer, free falling cone (Graviprobe), tunning fork (Rheotune), towing object (Rheocable), (Kiricheck et al., 2018)

can be determined with use of seismics, with pressure waves (P-waves) and shear waves (S-waves). This task is not straight forward, since water is a fluid and therefore S-waves will not propagate through it.
Drijkoningen et al. (2012) showed that under certain conditions marine streams can contain S-wave arrivals. These are converted P- to S-waves. This could have great potential since it allows one to derive shear parameters without the need of having sources or receiver being in contact with the fluid mud.
In this thesis, I will investigate if shear parameters in fluid mud can be derived with S-waves and with P-waves if an array is used, and which frequencies are most effective in doing so.
The main research question posed is as follow: *How can shear parameters, such as shear modulus be linked to yield stress in fluid mud?*
To answer this question the following sub-questions have to be answered:

1. How do P-wave and S-wave velocities differ in fluid mud with respect to time for different mud samples?
2. How do p and S-waves vary with varying density and frequency?
3. How are S-wave velocities and shear parameters linked to the yield stress of fluid mud?
4. How to determine shear parameters and what geometry is required to measure the shear parameters in fluid mud?

In order to investigate this, I conduct a lab experiment at Deltares and TU Delft from which I will estimate the seismic velocities. This is done in a controlled environment with fluid mud with a known volume. At Deltares, I also measure the rheologic parameters of the mud samples to link to the results of the seismic experiments.
The idea of how to derive the yield stress of the fluid mud is as follows:

1. Derive P- and S-wave velocities for different types of fluid mud with different densities and use different frequencies.
2. Calculate the density and shear modules.
3. Use the available lab equipment (rheometer) to measure the yield stress of the fluid mud.
4. Derive a relation between yield stress and seismic velocities.

Due to a time constrain, this is only done for a small part of the PoR. This part can be seen in Figure 1.2. Figure 1.2 also shows where the two mud samples have been acquired: in the 7th Petroleum Harbor and in the Caland Channel. The main difference between these samples is the organic matter. This is important to note since organic matter is related to gas production and gas affects seismic velocities.

Figure 1.2: Map of the sampling locations in the 7th Petroleum Harbor in red and in green the sampling location for the Caland channel. The sample from the 7th Petroleum Harbor was taken next to a small platform. (Retrieved from Google Maps on 30-07-2019)

2

Theory

In this chapter, I explain the theory behind the lab experiments. It contains a detailed explanation of how seismic velocities are related to shear strength and density. I also explain how attenuation depends on rheological properties.

2.1. Seimic velocities

In order to determine the shear modulus, we need to know the P- and S-wave velocities. The P-wave velocity is given by

$$c_p = \sqrt{\frac{\lambda + 2\mu}{\rho}} \tag{2.1}$$

and the S-wave velocity is given by

$$c_s = \sqrt{\frac{\mu}{\rho}} \tag{2.2}$$

where λ, μ, and ρ stand for the Lamé parameters, shear modulus and density, as described in Wapenaar (1989). Figure2.1 illustrate the P- and S-wave propagation.

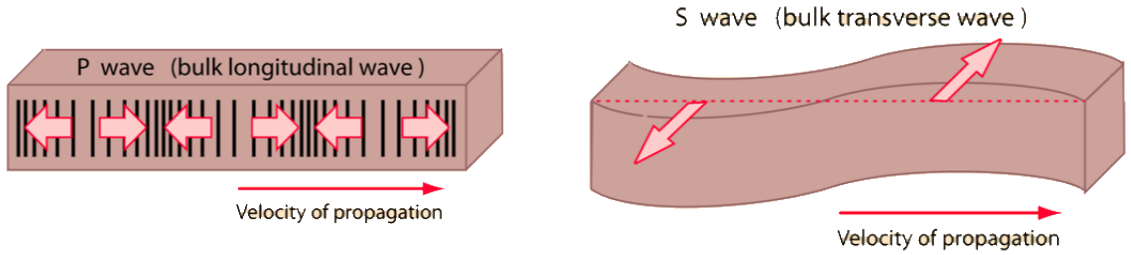

(a) S-wave illustration

Figure 2.1: P-wave propagation on the left and S-wave propagation on the right

When we would consider an ideal fluid, with $\mu = 0$, then there will be no S-wave, as can be seen from Equation 2.2. In contrast to S-waves, P-waves will propagate through a medium with a shear modulus being equal to 0. Fluid mud has low shear modulus. As a consequence, we need to solve for both P- and S-waves propagation, which adds complexity compared to the ideal fluid case where $\mu = 0$.

For reasons of simplicity, I assume that my liquids are homogeneous and isotropic. This assumption can be justified since the fluids get mixed and sedimentate and consolidate undisturbed, thus homogeneous fluids were used for all the experiments.
Since fluids are considered, λ is expressed in shear modulus μ and bulk modulus K which results in:

$$\lambda = K - \frac{2}{3}\mu. \tag{2.3}$$

When we substitute Equation 2.3 into Equation 2.1, and using the the expression for P- and S-wave velocity in Equation 2.1 and 2.2, we can express the bulk modulus and shear modulus in terms of P- and S-wave velocities meaning

$$\frac{c_p^2}{c_s^2} = K\frac{1}{\mu} + \frac{4}{3}. \tag{2.4}$$

This equation allows us to derive the bulk modulus if the P- and S-wave velocities are known for a fluid with a known density.
For a transmission measurement, calculation of the P- and S-wave velocity is relatively straight forward since the path is know. With reflection measurements, one needs to take the angle of incidence into account.

2.1.1. Acoustic waves in lossless fluids

The linearized Equation of motion for acoustic waves (P-waves only) in a lossless non-flowing fluid is described by Wapenaar, (n.d.) according to

$$\rho\frac{\partial v}{\partial t} + \frac{\partial p}{\partial x_i} = f_i, \tag{2.5}$$

with ρ representing density, v velocity, t time, p pressure, f_i an external force, and x_i the spatial coördinates with subscribt i= 1,2 or 3, denoting the dimensions. Equation 2.5 relates the velocity field v in any medium $x \in G \subset R^3$ with $t \in [t_o, t_1] \subset R$ to its mass density ρ, pressure field p, and external force f. The linearized stress-strain relation can be described as

$$k\frac{\partial p}{\partial t} + \frac{\partial v_i}{\partial x_i} = q. \tag{2.6}$$

Here, q represents the force density function or volume mass injection function, meaning the in and/or out flow of a volume. By elimination v_i from Equations 2.5 and 2.6, we get the acoustic wave equation according to:

$$\rho\frac{\partial}{\partial x_i}\left(\frac{1}{\rho}\frac{\partial p}{\partial x_i}\right) - \frac{1}{c^2}\frac{\partial^2 p}{\partial t^2} = \rho\frac{\partial}{\partial x_i}\left(\frac{f_i}{\rho}\right) - \rho\frac{\partial q}{\partial t}, \tag{2.7}$$

where c is the acoustic propagation velocity defined as in Equations 2.1. However, since we consider a fluid, λ is substituted according to Equation 2.3 and if we consider μ =0, meaning we do not take shear strength into account, we get:

$$c_p = \sqrt{\frac{k}{\rho}}. \tag{2.8}$$

This could hold for P-waves since the acoustic velocity will predominately depend on the compressibility of the fluid mud due to its weak structure.
If we consider ρ to be constant, implying for a homogenous medium, then Equation 2.7 reduces to:

$$\frac{\partial}{\partial x_i}\frac{\partial p}{\partial x_i} - \frac{1}{c^2}\frac{\partial^2 p}{\partial t^2} = \frac{\partial f_i}{\partial x_i} - \rho\frac{\partial q}{\partial t}. \tag{2.9}$$

2.1.2. Acoustic waves in dissaptative fluids

When a non-flowing liquid in relaxation is considered, Equation 2.5 and 2.6 can be extended according to De Hoop (1992) to:

$$\rho^r * \frac{\partial v}{\partial t} + \frac{\partial p}{\partial x_i} = f_i. \tag{2.10}$$

Here $\rho^r * \frac{\partial v}{\partial t}$ stands for a temporal convolution, with $\rho^r = \rho(\mathbf{x}, t)$. Since only causal times are considered, (t > 0), $\rho^r(\mathbf{x}, t) = 0$ for t < 0. The subscript ^{r} stands for a medium in relaxation, the * denotes a complex conjugate. This leads to ρ^r representing the mass-density relaxation function. Similar to the extension of Equation 2.5 to Equation 2.10, Equation 2.6 can be extended to:

$$k^r * \frac{\partial p}{\partial t} + \frac{\partial v_i}{\partial x_i} = q. \tag{2.11}$$

Here $k^r(\mathbf{x}, t)$ represents the compressibility relaxation function.
Since fluid mud is in relaxation, the compressibility and mass density can be drescribed as a function of time. Unlike fluid mud, consolidated mud does not exhibt relaxation. Therefore, $\rho^r(\mathbf{x}, t) = \rho(\mathbf{x})\delta(t)$ and $k^r * (\mathbf{x}, t) = k(\mathbf{x})\delta(t)$. This implies that Equations 2.10 and 2.11 would simplify according to Equation 2.6 and Equation 2.7
If a medium without a source is considered, Equations 2.10 and 2.11 can be re written according to Equation 2.12 and 2.13.

$$\frac{\partial p(\mathbf{x}, t)}{\partial x_i} = \int_{-\infty}^{t} \rho^r(x, t - t') \frac{\partial v(\mathbf{x}, t')}{\partial t'} dt' \tag{2.12}$$

$$\frac{\partial v(\mathbf{x}, t)}{\partial x_i} = \int_{-\infty}^{t} k^r(x, t - t') \frac{\partial p(\mathbf{x}, t')}{\partial t'} dt' \tag{2.13}$$

Equations 2.12 and 2.13 are used to express that the changes in space, $\partial p(\mathbf{x}, t)/\partial x_i$ and $\partial v(\mathbf{x}, t)/\partial x_i$ are dependent on the complete history of the fluid's change in time, $\partial v_i(\mathbf{x}, t)/\partial t$ and $\partial p(\mathbf{x}, t)/\partial t$.
Likewise, the change in time, $\partial v_i(\mathbf{x}, t)/\partial t$ and $\partial p(\mathbf{x}, t)/\partial t$ can be expressed in changes in space, $\partial p(\mathbf{x}, t)/\partial x_i$ and $\partial v(\mathbf{x}, t)/\partial x_i$ resulting in Equation 2.14 and 2.15, respectively.

$$\frac{\partial v(\mathbf{x}, t)}{\partial t} = \int_{-\infty}^{t} l^r(x, t - t') \frac{\partial p(\mathbf{x}, t')}{\partial x_i} dt' \tag{2.14}$$

$$\frac{\partial p(\mathbf{x}, t)}{\partial t} = \int_{-\infty}^{t} K^r(x, t - t') \frac{\partial v(\mathbf{x}, x_i)}{\partial t'} dt' \tag{2.15}$$

In Equations 2.14 and 2.15, $l^r(\mathbf{x}, t)$ and $K^r(\mathbf{x}, t)$ represent the inverse of $\rho^r(\mathbf{x}, t)$ $k^r(\mathbf{x}, t)$ which we can call the lightness relaxation function and the compression-modulus relaxation function. The parameters $l^r(\mathbf{x}, t)$ and $K^r(\mathbf{x}, t)$ are the inverse of $\rho^r(\mathbf{x}, t)$ and $k^r(\mathbf{x}, t)$ according to:

$$\delta(t) = l^r(\mathbf{x}, t) * \rho^r(\mathbf{x}, t) = \int_0^t l^r(x, t - t')\rho^r(\mathbf{x}, t')dt' \tag{2.16}$$

$$\delta(t) = K^r(\mathbf{x}, t) * k^r(\mathbf{x}, t) = \int_0^t l^r(x, t - t')k^r(\mathbf{x}, t')dt'. \tag{2.17}$$

Like $\rho^r(\mathbf{x}, t)$ and $k^r(\mathbf{x}, t)$, $l^r(\mathbf{x}, t)$ and $K^r(\mathbf{x}, t)$ must be a causal function of time. This is a necessary condition for a physical fluid; however, this is not sufficient since energy dissipation is not considered. Energy dissipation will be considered in the next section. Also note that all the equations are only valid for a time t < time for the mud to go from fluid mud to consolidated mud. The reason for this, is that mud is no longer in relaxation in the phase after fluid mud, which is the (pre)-consolidated phase.

2.1.3. Kevin-Voigt

Fluid mud is viscoelastic, meaning that when a stress σ is applied, the response is in terms of strain ε, which is hampered by the stiffness of the spring E, and viscous damper η. This response is illustrated in Figure 2.2. The Kelvin-Voight model assumes that the stress experienced by both components, the spring and the dashpot, is the same. This leads to $\sigma_t = \sigma_s + \sigma_d$, with the subscripts $_{t,s}$, and $_d$ representing the total stress, the stress experienced by the spring, and the stress experienced by the dashpot.
In this model, the strain in the spring and dashpot is experesed as:

$$\varepsilon = \frac{1}{E}\sigma_s, \frac{\partial \varepsilon}{\partial t} = \frac{1}{\eta}\sigma_d. \tag{2.18}$$

By eliminating of σ_s and σ_d and using the dot notation, we get the Kelvin-Voigt Model as according to Equation 2.19.

$$\sigma_t = E\varepsilon + \eta\dot{\varepsilon} \tag{2.19}$$

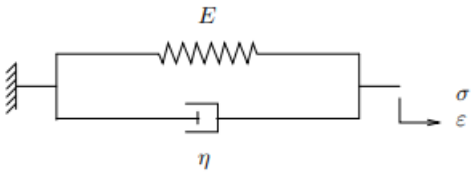

Figure 2.2: Illustration of the Kelvin-Voigt model where the stress-strain is described by the response of a spring in E and the response of a dash-pot in η to a stress σ.

It is important to note the damping effect of the viscosity is temperature- and frequency-dependent; however, this thesis only focuses on the frequency dependency $\eta(\lambda)$.
The Kelvin-Voigt model considers the storage modulus $G'(\lambda)$ to be a constant function of λ, whereas the loss modulus $G"(\lambda)$ scales linearly with λ ((Lewandowski & Chorążyczewski, 2010). This will be further elaborated in Section 2.4

This model allows us to define our above-defined parameters $l^r(\mathbf{x},t)$ and $K^r(\mathbf{x},t)$ and their inverse versions as according to Equation 2.20 and 2.21

$$l^r(\mathbf{x},t) = l(\mathbf{x})\delta(t) + \zeta(\mathbf{x})\dot{\delta}(t) \tag{2.20}$$

$$K^r(\mathbf{x},t) = K(\mathbf{x})\delta(t) + \eta(\mathbf{x})\dot{\delta}(t) \tag{2.21}$$

and the inverse versions as according to Equation 2.22 and 2.23.

$$\rho^r(\mathbf{x},t) = \frac{H(t)}{\zeta(\mathbf{x})}\exp(-\frac{l(\mathbf{x})}{\zeta(\mathbf{x})}t) \tag{2.22}$$

$$k^r(\mathbf{x},t) = \frac{H(t)}{\eta(\mathbf{x})}\exp(-\frac{K(\mathbf{x})}{\eta(\mathbf{x})}t) \tag{2.23}$$

where $\zeta(\mathbf{x})$ and $\eta(\mathbf{x})$ are the inverse friction coefficient and the **inverse** viscosity.
When we use these two parameters defined in Equations 2.22 and 2.23, and substitude them into Equations 2.14 and 2.15, then this leads to

$$\frac{\partial v_i(\mathbf{x},t)}{\partial t} = -l(\mathbf{x})\frac{\partial p(\mathbf{x},t)}{\partial x_i} - \zeta(\mathbf{x})\frac{\partial}{\partial t}\frac{\partial p(\mathbf{x},t)}{\partial x_i} \tag{2.24}$$

$$\frac{\partial p(\mathbf{x},t)}{\partial t} = -K(\mathbf{x})\frac{\partial p(\mathbf{x},t)}{\partial x_i} - \eta(\mathbf{x})\frac{\partial}{\partial t}\frac{\partial v_i(\mathbf{x},t)}{\partial x_i} \tag{2.25}$$

which now does account for losses. If we now integrate Equation 2.25 with respect to time then this results in

$$p(\mathbf{x},t) = -K(\mathbf{x})\frac{\partial u_i(\mathbf{x},t)}{\partial x_i} - \eta(\mathbf{x})\frac{\partial v_i(\mathbf{x},t)}{\partial x_i}, \tag{2.26}$$

with $u_i(\mathbf{x},t)$ is equal to the particle displacement. For detailed derivations of the above equation regarding acoustic wave propagation with losses according to the the Kelvin-Voigt model, the reader is referred to Dahlen & Tromp (1998).
Finally, when we eliminate v_i from Equation 2.10 and Equation 2.6 with use of Equation 2.16, we get the wave equation for a dissipative fluid according to Equation 2.27

$$\frac{\partial}{\partial x_i}(l^r * \frac{\partial p}{\partial x_i}) - k^r * \frac{\partial^2 p}{\partial t^2} = \frac{\partial}{\partial x_i}(l^r * f_i) - \frac{\partial q}{\partial t} \tag{2.27}$$

which reduces for a homogeneous fluid to

$$\frac{\partial}{\partial x_i}\frac{\partial p}{\partial x_i} - \rho^r * k^r * \frac{\partial^2 p}{\partial t^2} = \frac{\partial f_i}{\partial x_i} - \rho^r * \frac{\partial q}{\partial t} \tag{2.28}$$

according to Wapenaar (n.d.).
Equation 2.28 will be further extended to the elastic wave equation in the next section.

2.1.4. Elastic waves

In order to simulate both P- and S-waves in a model space $\mathbf{m}$, we need to further extend the wave equation Equation 2.28 in the previous section to the elastic wave equation. This is done by adding S-waves which results in the elastic wave Equation 2.29

$$\rho(\mathbf{x})\ddot{u}(\mathbf{x},t) - \nabla \times \sigma(\mathbf{x},t) = \mathbf{f}(\mathbf{x},t), \quad x \in G \subset R^2 \tag{2.29}$$

that relates the displacement field $\mathbf{u}$ in our 2D domain $G \subset R^2$ to the mass density ρ, the 2 by 2 stress tensor σ and source function f for any causal time (Dahlen & Tromp, 1998 and Kenneth, 2001). Note that here I dropped the attenuation factors making it a lossless wave propagation equation. Equation 2.29 is used to model wave propagation with a Finite Difference scheme and an attenuation factor. This attenuation factor is derived by fitting synthetic seismogram to the seismogram acquired from the lab experiments, implying it is a constant quality factor, and not material specifically defined.

The shear wave velocity is given by Equation 2.30.

$$c_s = \sqrt{\frac{\mu}{\rho}} \tag{2.30}$$

In ideal fluids, such as pure water, there is no shear strength which can support the propagation of S-waves. Therefore S-waves will not propagate through a fluid as such. This results in the wave equation to be according to Equation 2.28.
Fluid mud has some shear strength, <2kPa, and is therefore able to support S-waves.

P-waves are capable of propagating through ideal fluids, meaning that the particle velocity is curl-free. Opposed to this, the particle velocity is not divergence free.
S-wave particle velocity on the other hand is divergence free, but not curl free. This leads to the following relations:

$$\nabla \cdot v_p = 0. \tag{2.31}$$

$$\nabla \times v_s = 0 \tag{2.32}$$

In Equations 2.31 and 2.32 fundamental properties of the elastic wave motion are defined according to Wapenaar (1989). This also determines. They determine the amount of unknowns that have to be computed.

2.1.5. Signal attenuation

Seismic-signal attenuation is linked to scatter and absorption. This happens first inside the fluid. However, the attenuation processes due to the inhhomogeneities inside the fluids are the main interest to determine the rheological properties of fluid mud. The signal attenuation with respect to absorption is linked to heat conduction and viscosity (Allegra and Hawley, 1972). For fluid mud, thermal losses are very small as described by Haw and Burling (1982). Viscous absorption affects the attenuation in a more seriously, but it still only contributes to a few percent of the signal attenuation (Hay and Mercer, 1985). The cause of signal attenuation is predominantly caused by scatter.
My preliminary results (first rough velocity estimates of the lab experiments) indicate that the minimum c_p and c_s range from 1500 - 1600 and 600 - 1100 and higher for a frequency of 1 Mhz, respectively. Equation 2.33 allows us to determine the minimum wavelength for a known frequency f and velocity C. $\lambda_p min$ is likely to be ≈ 1.5 mm, $\lambda_s min$ is likely to be ≈ 0.6 mm. This implies that P-wave scattering will be Rayleigh scattering for fluid mud consisting of grains only smaller than gravel (grain size 2-4 mm). For S-wave scattering, also mie scattering or non-selective scattering could occur if the fluid mud has grains equal or larger than 0.6 mm which corresponds to coarse sands. However, it is very likely that the dominant type of scattering is still Rayleigh scattering since the grain size of fluid mud is generally much smaller than even 2 mm.

$$\lambda = \frac{C}{f} \tag{2.33}$$

2.1.6. Dispersion

It is important to investigate the dispersion due to the use of different frequencies, as will be discussed in the results section. Dispersion relates to the increase in velocity with increase in frequency. By using the Kramers-Kroning relation or integral dispersion relation, the dispersion behavior can be modeled (Oestreicher, 1951; Blackstock, 2001), and some physical properties could be derived from this behavior (Donoghue, 1995 ; Barry et al., 2012), potentially even properties such as viscosity and elasticity (Chen, Fatemi and Greenleaf, 2004).
To determine the dispersion from S-waves in fluid mud, mutiple frequencies will be used, as described in the next section. The velocities of these different frequencies will be analyzed and a dispersion curve will be calculated from these velocities.

2.2. Seismic lab measurements

For this thesis, I conducted transmission measurements and reflection measurements. The dimensions of the container and the electrical setup can be seen in Figure 2.3 and a picture of the cylinder with the transducers mounted on it can be seen in Figure 2.4 . Transmission measurements are conducted to estimate the seismic velocities in fluid mud over time. It is assumed that the fluid is homogeneous and that the density can be approximated since the initial volume is known and the water/mud interface can be measured. A cylinder is used for these measurements since this will using reflections under a 45 degree angle as a quality control. In addition to the transmission measurements, reflection measurements were conducted. The main difference between the reflection measurements and the transmission measurements is that the reflection measurement is more representative for real applications in the PoR.
I used multiple frequencies for the transmission measurements: 200 kHz, 300 kHz, 400 kHz, 500 kHz, 600 kHz, 800 kHz, and 1 MHz. This range allows determining a dispersion curve and to conduct a frequency analysis. Furthermore, it gives insights into which frequency to use on a small scale to get a maximum signal-to-noise ratio.
Extending the range below 200kHz was undesirable since the amplifier that I used distorted the source signal substantially below 200 kHz, while it started buzzing above 1 MHz.
The reflection measurements will be further discussed in the next sub-chapter. A schematic overview of the seismic experiment setup can be seen in Figure 2.3

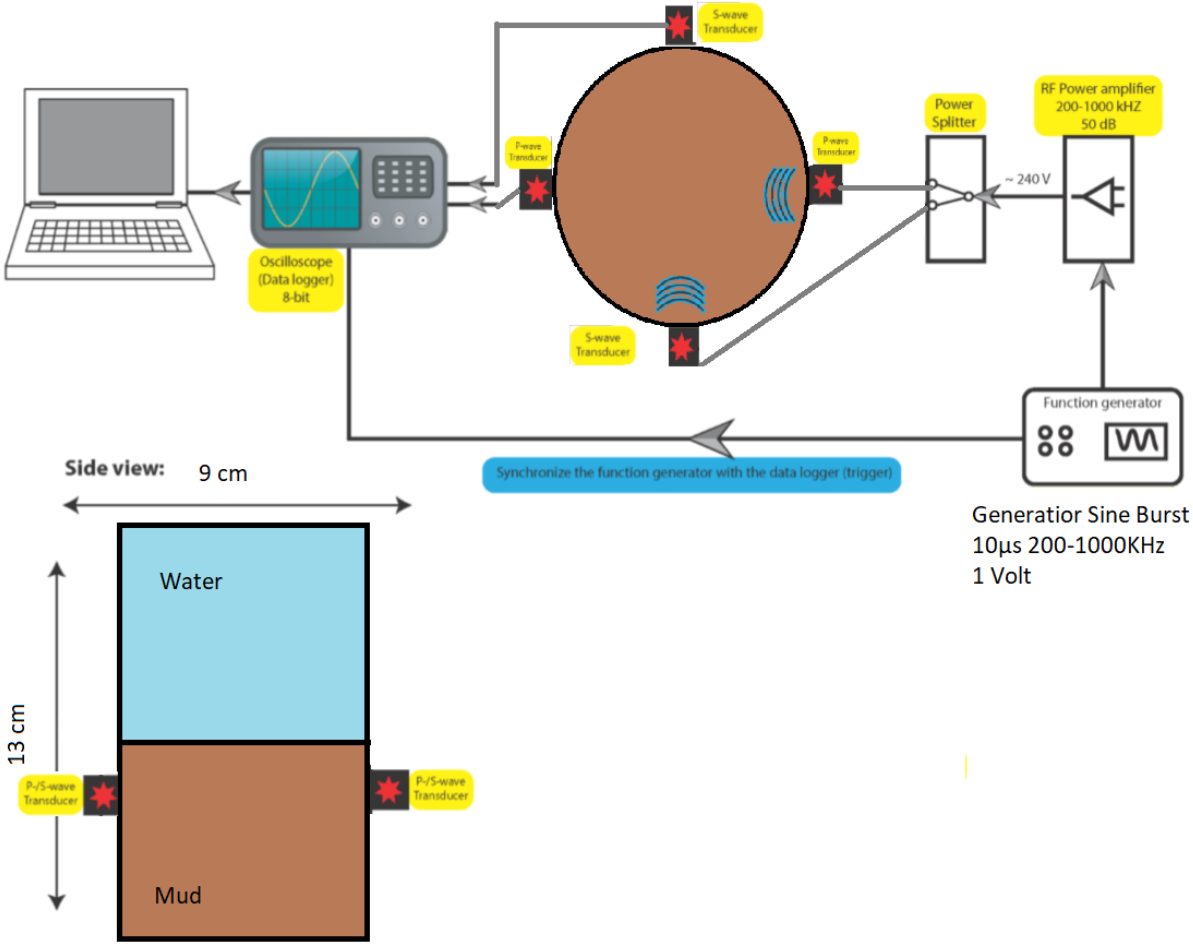

Figure 2.3: The setup of the seismic experiment for the transmission measurements. Note that the S- and P-wave transducers can act both as source and receivers.

Figure 2.4: Photo of the cylinder used to estimate P- and S-wave velocities

2.3. Reflection measurements

In addition to the transmission measurements, I also conducted reflection measurements. This is done with two transducers with a source frequency of 100 kHz. The source transducer is fixed and the receiver transducer is moved manually by a fixed offset to mimic as if it would be an array of receivers.
The reason for this lower frequency, with respect to the frequencies used for the transmission measurements, is because the aim of the reflection measurements is to detect a Scholte wave and converted P- to S-waves. This can theoretically only be done with an offset shorter than 0.0039 m with a velocity of 1560 [m/s] and frequency of 100 kHz to prevent aliasing. But by decreasing the offset even further to 0.002 m, it would be easier to pick the Scholte wave and converted P- to S-waves. When the frequency would be higher, 500 kHz for example, the theoretical height limit would be 0.000078 m or 0.78 mm which is far too difficult to shift manually. The first setup can be seen in Figure 2.5.
The second setup is with both transducers at an angle of 30 degrees slightly above the water/mud interface. Here the aim was to detect converted P- to S-waves.

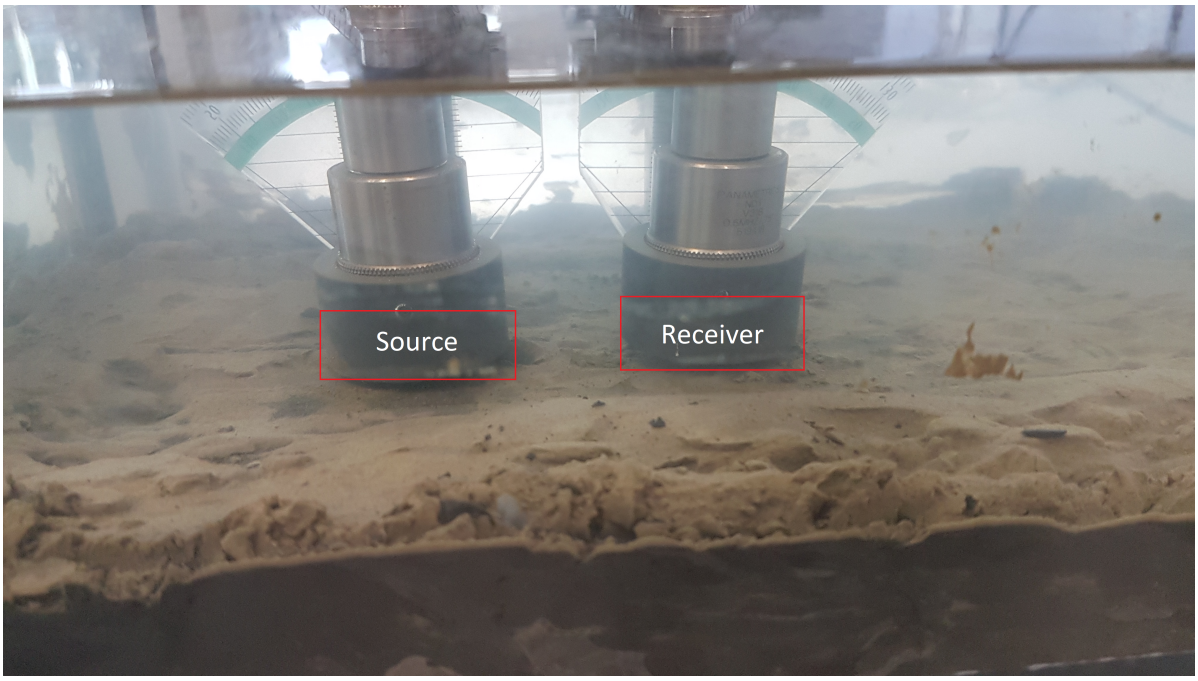

Figure 2.5: Measurement setup for the first trace. The first offset from the middle of the source transducer to the middle of the receiver transducer is 5 cm. The diameter of the transducer is 1.5 cm. After the first measurement the receiver is shifted manually by 2 mm. Above the red square is the plate of the transducer, meaning that everything in the red square is part of the mount and is not part of the transducer itself.

2.4. Determining the static yield stress

To asses the yield point from the fluid mud from the PoR, a lab experiment has been conducted. For this experiment, a rotational rheometer is used. With the rheometer, a steady sweep test, an oscillation test, and a frequancy test is conducted. All the tests were conducted at 20 °C. This temperature has been chosen for convenience since the laboratory where the measurements were conducted, is regulated at 20 °C. A temperature of around 14 °C would be more desirable since this is closer to the average water temperature (RWS, 2017); however due to the limited resources available for cooling the seismic experiment, this was not possible.

The steady sweep test is used to determine the viscosity of the fluid, which is defined in Equation 2.36, in which η represents viscosity in [mPas]. This is calculated by determing the shear stress τ in N/m^2 according to Equation 2.34, where F represents shear force in Newtons [N] and A area in m^2 and shear rate $\dot{\gamma}$ in 1 s^-1, reciprocal seconds, according to Equation 2.35 where υ represents velocity and h a known gap in [m].

$$\tau = \frac{F}{A} \tag{2.34}$$

$$\dot{\gamma} = \frac{\upsilon}{h} \tag{2.35}$$

$$\eta = \frac{\tau}{\dot{\gamma}} \tag{2.36}$$

The oscillation test is used to determine the phase angle δ, which is an indicator of the fluid's structure strength, which is described in terms of the complex shear modulus G^* composed of the real part, the storage modulus *G'*, and the imaginary part, the loss modulus ,*G"*. *G'* is the ratio between the stress to strain that is in phase, which is the elastic component. *G"* represents the ratio between stress to strain of the viscous component which is out of phase (Mason & Weitz, 1995). These moduli need to be known to determine the shear strength mechanically.

To determine the relative contribution between *G'* and *G"* a frequency swipe test is preformed with different frequencies. This is done because the *G'* and *G"* are frequency depend (Mason & Weitz, 1995). The frequency used to derive the storage modulus and loss modulus is 1 Hz.

2.4.1. Herschel-Bulkley fluid

Fluid mud is is likely best described by a Herschel-Bulkley, which is illustrated in Figure 2.6, fluid model (also commonly referred to as Yield-Power-Law). This model is chosen due to fluid mud's shear thinning behavior. Shear thinning can also be described with a Bingham-plastic model, which is also illustrated in Figure 2.6; however, a Herschel-Bulkley would yield beter results in general (Santanu et al., 1994 ; Hemphill et al., 1993) when adequate data are available. The Herschel-Bulkley model is very similar to the Yield-Power-Law model, with the addition of an initial shear stress value, as illustrated in Figure 2.6. It can be described by Equation 2.37. Figure 2.6 serves for illustration purposes for these models.

$$\tau = \tau_0 + c\gamma^n \tag{2.37}$$

In Equation 2.37 τ represents the yield point, τ_0 initial fluid yield point with a shear rate=0, c consistency index, γ shear rate, and n Power-Law index. The yield point is defined as a critical level of stress below the point of which a material behaves elastically, like a solid, and above this point, the structure breaks down and the material starts flowing.

For a Herschel-Bulkley fluid, the stress-strain relation is non-linear, unlike in a Newtonian fluid. This can also be seen in Equation 2.37. In fluid mud, shear thinning occurs when the shear rate increases. Therefore, determining the yield point is more challenging than if it were a Newtonian fluid. Also the fluid flow behavior is different. Non-Newtonian fluids in general flow slower than a Newtonian fluid and the velocity decays faster (Huang & Garcia, 1997).

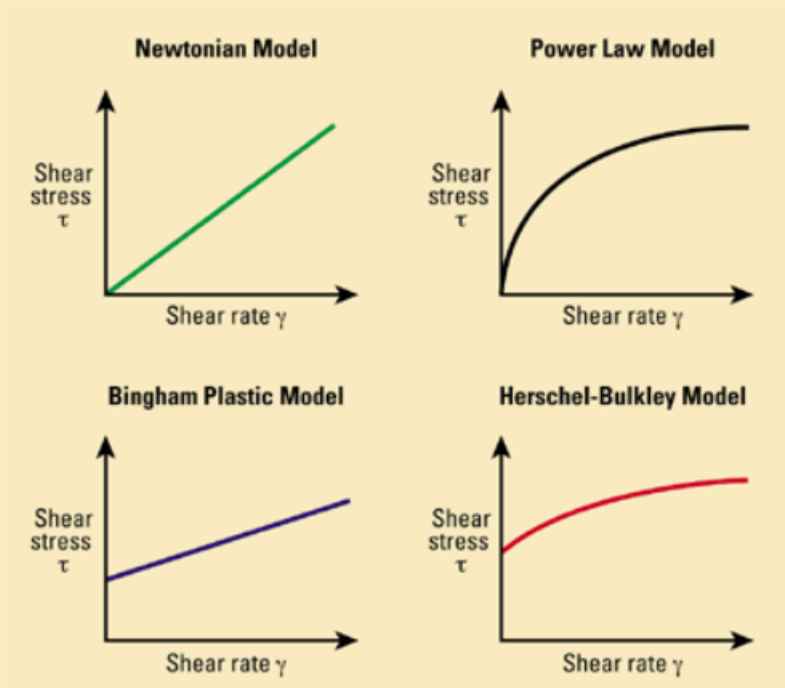

Figure 2.6: Illustration of the different fluid models. Retrieved from `https://www.glossary.oilfield.slb.com/en/Terms/h/herschel-bulkley_fluid.aspx` accessed 5-April-2019

3

Results

In this section, the results from the seismic measurements, forward models, and rheological measurements will be given.

3.1. Scattering with respect ot particle size

With the use of a Particle Distribution System, I determined the particle size distribution (PSD) of the mud which can be viewed in Figure 3.1 for the mud sample of the 7th Petroleum Harbor and Figure 3.2 for the mud sample of the Caland channel. The mud consists predominantly (98%) out of particles < $200\mu m$ in both samples. Therefore the scattering in this type of fluid mud will be dominated by Rayleigh scattering, which is likely to be true for almost every type of fluid mud which is not situated in a very turbulent environment.
What is striking is that the accuracy of determining larger grain sizes seems to be significantly diminished in the sample taken from the 7th Petroleum Harbor. One logical explanation is that this is likely caused by plant fibres. These fibres are 'string' like, meaning that they have an angle dependency for when the laser hits the fibre to determine the scattering.

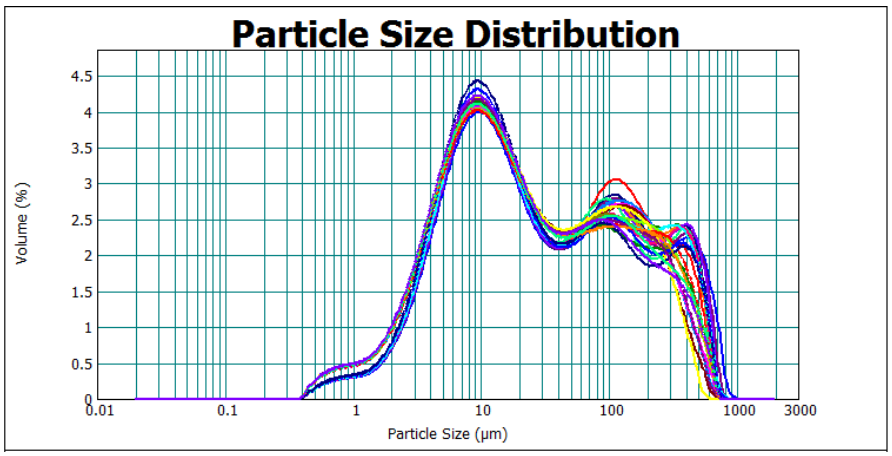

Figure 3.1: Particle size of the mud sample from the seventh Petroleum Harbor. Each colour represent one measurement to determine the grain size. Note that the irregularity is likely to be caused by organic fibres which are not perfect spheres and therefore give a large uncertainty since determining the size depends on the direction along which they are measured

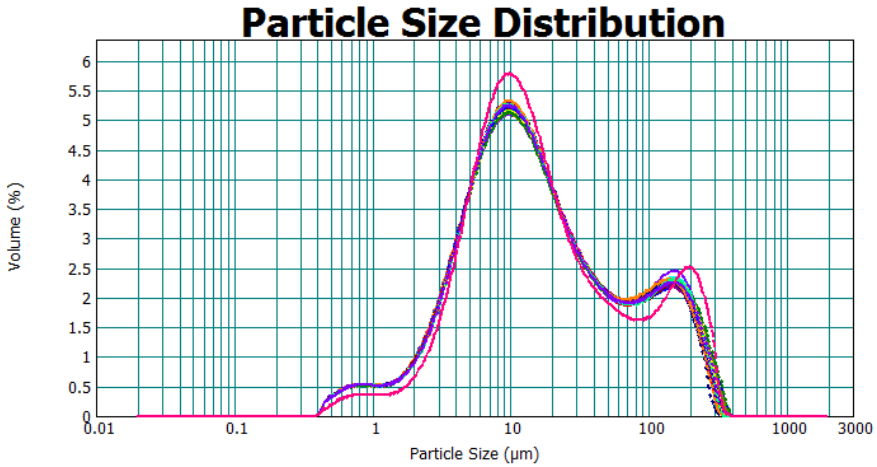

Figure 3.2: Particle size of the mud sample from the Caland channel. Each colour represents one measurement to determine the grain size.

3.1.1. Dispersion

An important part for numerical analysis, and the frequency analysis, is the dispersion. To determine the dispersion curve, I have conducted multiple measurements at different frequencies. Figures 3.3 and 3.4 show the dispersion curve for the P- and S-waves. Note that there are only seven data points and the frequencies range from 200 kHz to 1 mHz with a step of 100 kHz. Figures 3.3 and 3.4 show that the velocities differ substantially due to a change in frequency. This is important to note since the total increase in velocity due to sedimentation and consolidation is limited, which will be discussed in the next sections. What is also clearly visible is that the absolute difference in velocities, for both wave types, due to a change in frequency is about 20 m/s. This also means that the relative change in velocity due to a change in frequency is about one and half times larger for S-waves than for P-waves.

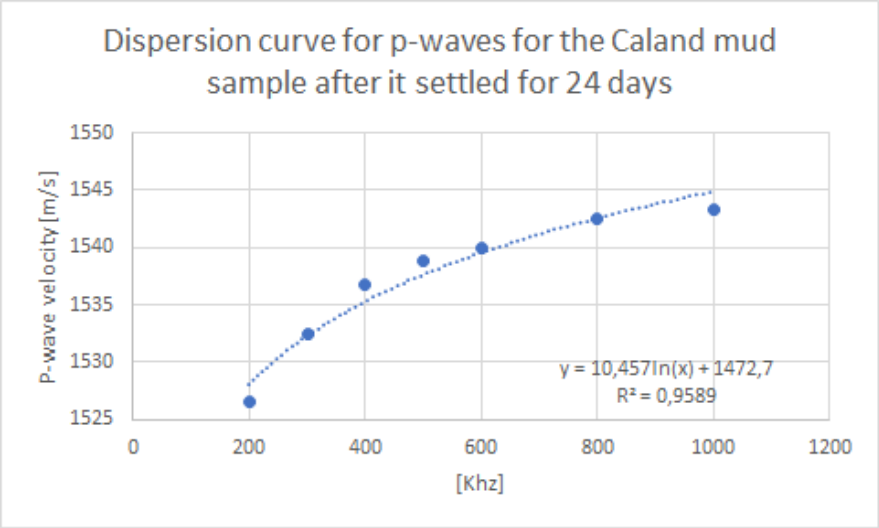

Figure 3.3: Dispersion curve for P-waves in fluid mud from the Caland Channel mud after 24 days. The largest amplitude in the P-wave arrival is used here instead of the first break for easy picking. The picking can be seen in Appendix A.2

It is likely dispersion differs per mud; however, the frequency analysis, which will be discussed further on, shows that this difference might be smaller than expected.

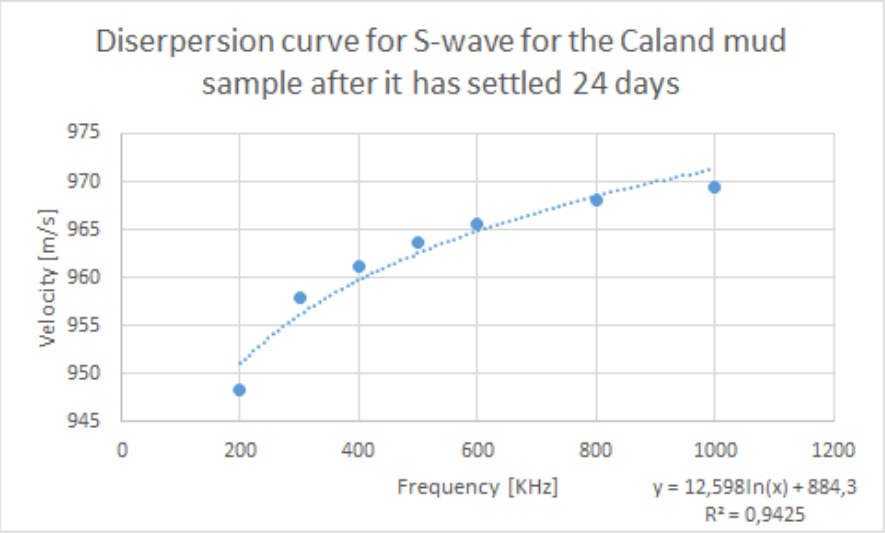

Figure 3.4: Dispersion curve for S-waves in fluid mud from the Caland Channel mud after 24 days. A clear arrival is used here instead of the first break for easy picking. The picking can be seen in Appendix A.1

3.2. P-wave velocities

In order to analyze the velocity-development of P-waves, I use the first arrival and the multiple. The first arrival is a good indicator for the P-wave velocity since it is the clearest arrival of all. However, due to the limited dimension of the cylinder from the transmission measurement, which is just 9 cm, and due to the limited change in P-wave velocities, picking the first arrival can lead to ambiguous results. By adding the multiple to the velocity analysis, the general velocity-development trend becomes clearer. Adding the multiple can only be done for the mud sample from the Caland channel since no clear multiple can be seen in the mud sample from the 7th Petroleum Harbor. These results can be seen in Figures 3.5, 3.6, 3.7, and 3.8.

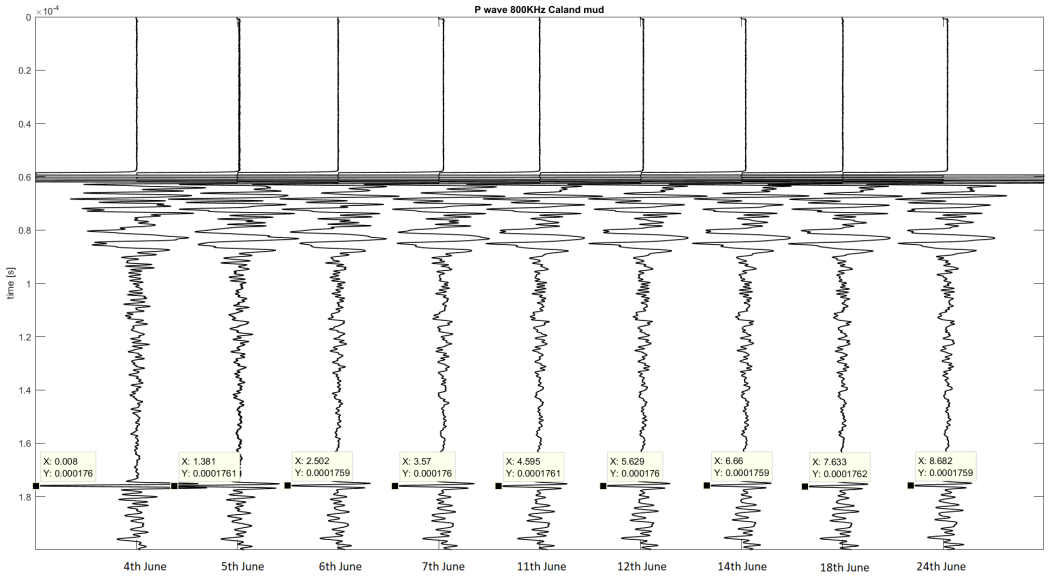

Figure 3.5: P-wave development in time from the Caland mud sample at 800 kHz. The first arrival is slightly before $6 * 10^{-5}$ seconds and the multiple is this time times 3. Note that the picking of the first arrival is different than the picking of the multiple. The reason for this is that for the first arrival it is easier to pick the first break whereas for the multiple this is more difficult due to noise.

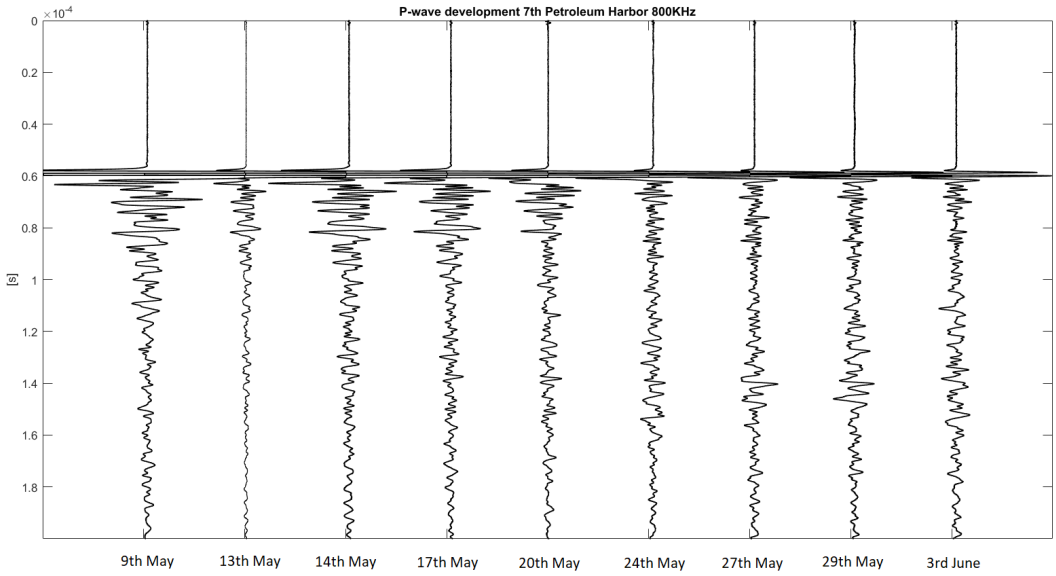

Figure 3.6: P-wave development in time from the 7th Petroleum Harbor mud sample with 800 kHz. The first arrival is slightly before $6 * 10^{-5}$ seconds. Note that the signal is more attenuated and therefore the mutiple is no longer clearly distinguishable.

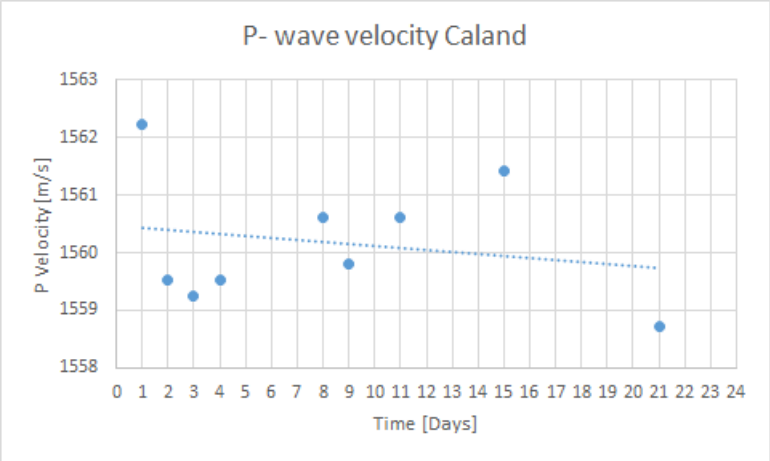

Figure 3.7: P-wave velocity-development from the Caland mud sample, 800 kHz used

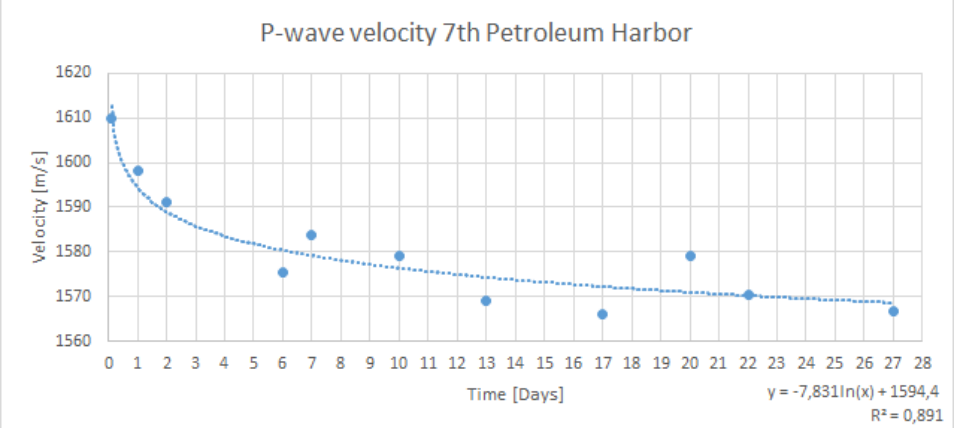

Figure 3.8: P-wave velocity-development from the 7th Petroleum harbor mud sample which contains a lot of organic material, 800 kHz used

In figure 3.7, there seems to be no clear trend. It seems as if there is a slight downward trend, but this is mainly caused by the first and last measurement. Figure 3.8 appears to have a downward trend in velocity. Also, the P-wave velocity in the mud from the 7th Petroleum in general appears to be higher than in the mud sample from the Caland Channel.

3.3. Shear waves

3.3.1. Identifying shear waves

Fluid mud is characterized by its low shear strength, making identifying S-waves challenging. Surprisingly enough, it is likely that shear waves can still be identified by correlating P-waves emitted by the S- transducers and P-waves emitted by the P- transducer. By comparing the results between this correlation and raw S-wave data, I get a correlation where the S-transducers emits P-waves and no correlation where the S- transducer emits S-waves.
Figure 3.9 shows the seismic traces measuring the wave propagation through fluid mud whose structure has completely been destroyed by stirring. Even though the structure has been completely destroyed, it seems that shear waves can still propagate through the fluid mud. For instance, it seems that there is an S-wave arrival at and before $1 * 10^{-4}$ second. If this is true, it would be very interesting since it means that 'fluid' mud is supporting shear waves far better than anticipated. In addition to this, it is very likely that shear velocities are much higher than shear velocity in for instance sand or in general soils, as will be described in the next section.
A major drawback is, however, that the even though it seems that a S-waves arrive somewhere between $0.9 * 10^{-4}$, it is challenging to pick the first break when it the development of the velocities and amplitudes over time is not shown, which will be shown in Figures 3.10 and 3.11 .

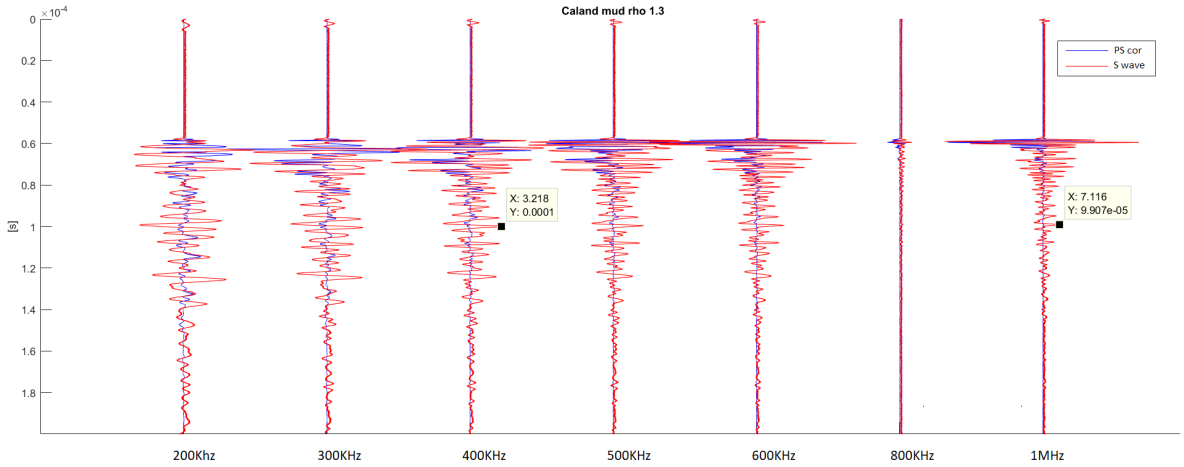

Figure 3.9: Seismic traces in fluid mud with a destroyed structure. In blue is the multiplication of the P-transducer signal with the S-transducer signal, leaving only the P-wave part emitted by the S-transducer. In red is the total signal emitted by the S-transducer. The measurement at 800 kHz has an amplitude problem which is likely caused due to a lower voltage input.

When the mud has been given some time to sedimentate and consolidate, the S-wave arrivals become more apparent, as can be seen in Figures 3.10 and 3.11. Picking the first breaks does become much simpler with a time series since one can zoom in and see the difference in arrival times between P- and S-waves with respect to time in days. By exploiting this difference in behavior over time, we can distinguish between P- and S arrivals, as can be seen in Figure 3.11. In Figure 3.11 the first break of the S-wave is compared with a clear P-wave reflection which allows for easy picking. This difference in arrival time over time could even allows us to pick the first break instead of a maximum amplitude.

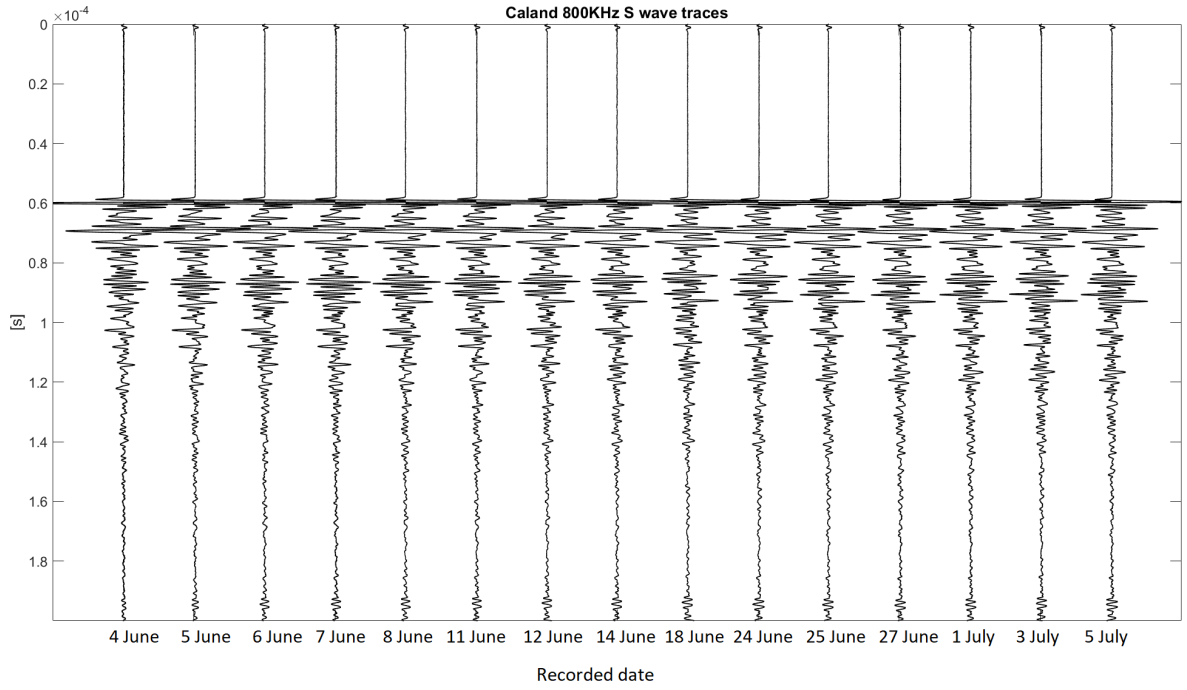

Figure 3.10: S-wave traces from the Caland mud sample with 800 kHz frequency. Note that besides an increase in velocity, meaning a decrease in travel time, there is also an increase in amplitude, especially in the first few days. This change is notable around

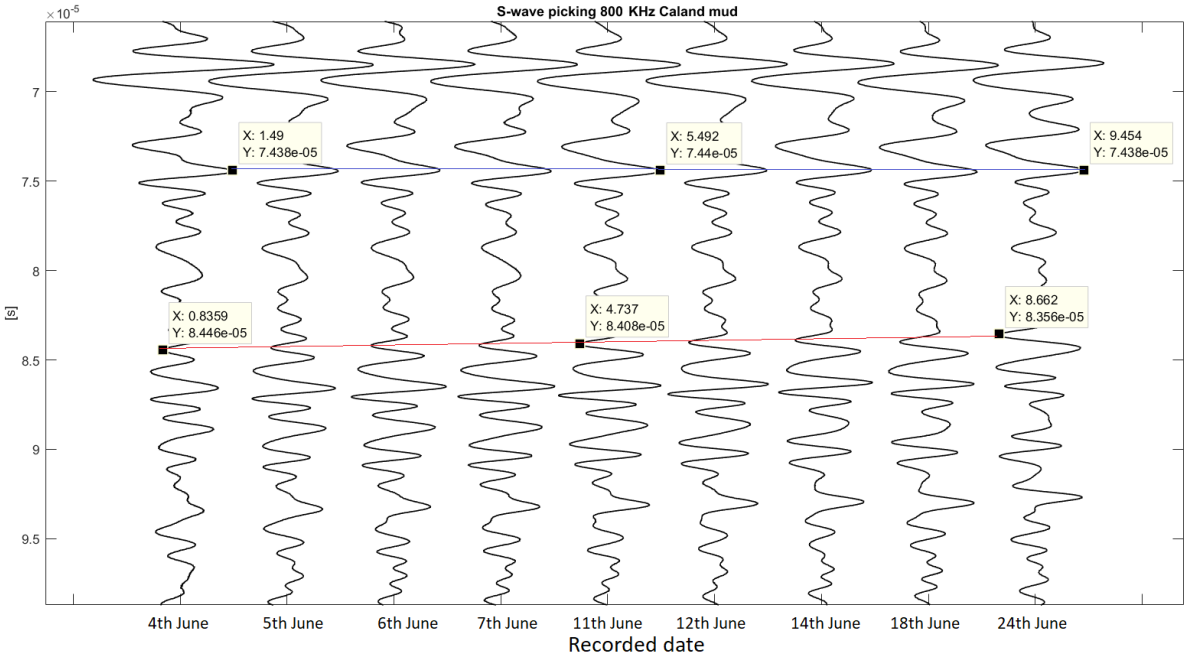

Figure 3.11: Difference in P-wave arrival times and S-wave arrival times with an 800 kHz source for mud from the Caland with a P-arrival with a large amplitude in blue and an S-arrival in red.

3.3.2. Shear velocities and shear modulus development

With time, the fluid mud starts to sedimentate and (pre)consolidate. This leads to shear thickening meaning it will be more resistant to movement. Due to an increase in shear strength, the shear velocity increased as expected. This can be seen in Figure 3.12. Besides an increase in velocity, also an increase in amplitude can be noticed in comparing the arrivals in Figures 3.10 compared and Figure 3.5 just below $0.8 * 10^{-4}$ seconds.

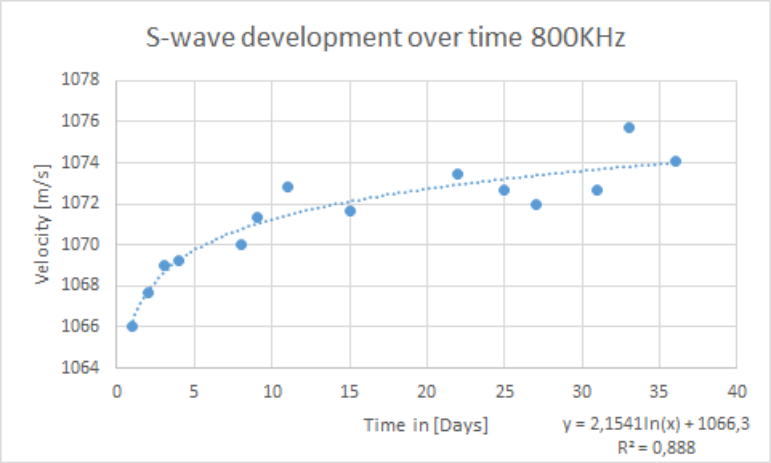

Figure 3.12: S-wave velocity-development over time for a source frequency of 800 kHz

Opposed to the unclear P-wave velocity trend from the Caland mud sample and the P-wave velocity decay trend from the 7th Petroleum Harbor, S-wave velocities show an exponential increase over time, as can be seen in Figures 3.7 and 3.8 compared to Figure 3.12.

3.4. Frequency analysis and center frequency

By transforming from the time domain to frequency domain, information regarding the frequencies can be derived. This allows determining the central frequency from different mud samples at different stages. The result can be seen in Figures 3.17 and 3.18 for the P- and S-wave frequency analysis, respectively.

3.4.1. P-wave frequency analysis

Since there is the possibility that a P-wave travels through the plastic of my cylinder and due to the clipping of the amplitude in the first break, only the time frame around the multiple has been chosen in the P-wave frequency analysis for the Caland mud. From the traces from the 7 Petroleum Harbor mud, there is no clear multiple visible. Here, I picked the first arrival from P-wave emitted by the S- transducer. The reason why I took the s receiver is because the amplitude is not clipped in the s receiver, opposed to the P- receiver.

The first striking result from the frequency analysis, is that it seems that the central frequency does not differ a lot for the two different mud samples. Also, it appears that the frequency spectrum does not differ a lot, if at all, between the two different time stages of the Caland mud sample. It appears that only the amplitude reduces.

Most importantly, it seems that the central frequency is around 380 kHz- 400 kHz. This is indicated by the results of a centre source frequency of 300, 400 ,and even 500 kHz it appears that the main frequency recorded is around 380 kHz-400 kHz.

Also, the lower frequencies are less attenuated, while the higher frequencies are more attenuated. That is, for a lower center frequency of the source, the recorded center frequency is closer to that of the source, while for the higher center frequencies of the source, the difference are much larger.

Furthermore, the relative change in recorded amplitudes with respect to time seems to be about the same for all centre source frequencies.

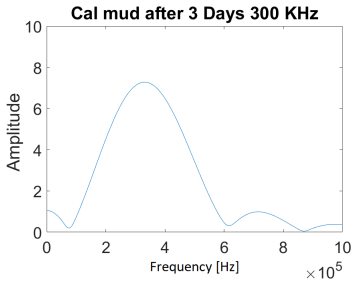

(a) 300 kHz source frequency spectrum after three days with the Caland mud

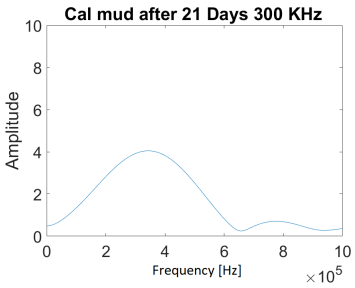

(b) 300 kHz source frequency spectrum after 21 days with Caland mud

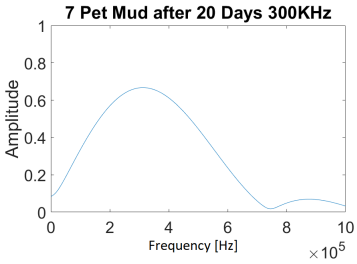

(c) 300 kHz source, frequency spectrum after 20 days with the 7th Petroleum Harbor mud day

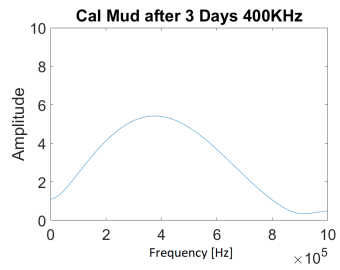

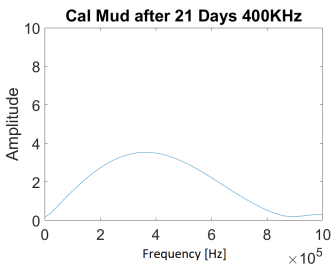

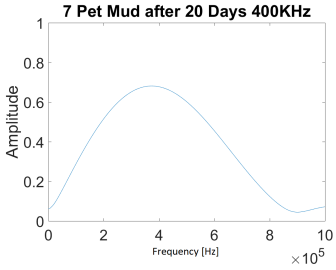

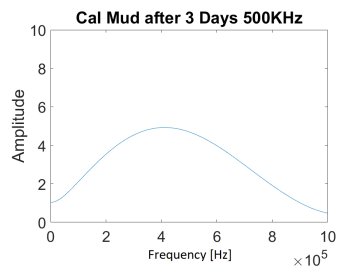

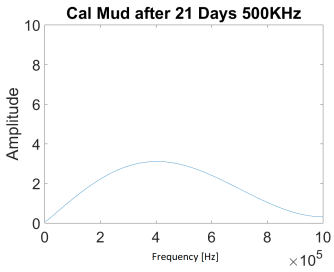

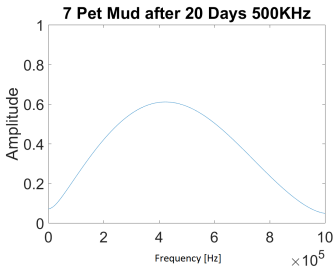

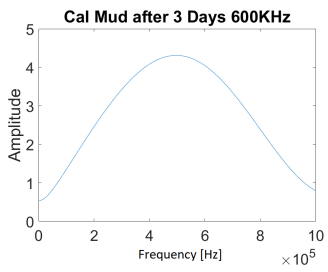

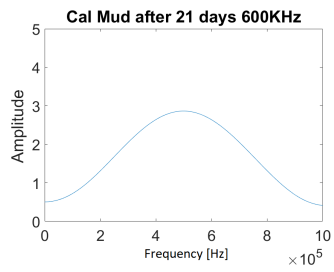

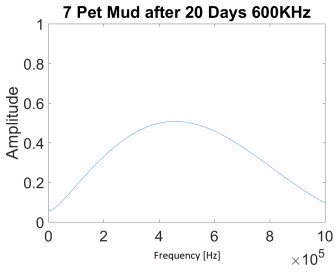

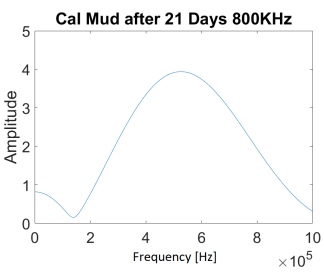

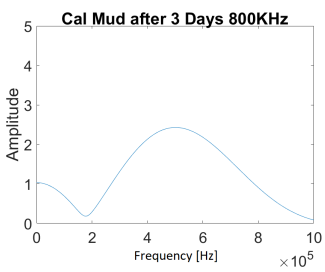

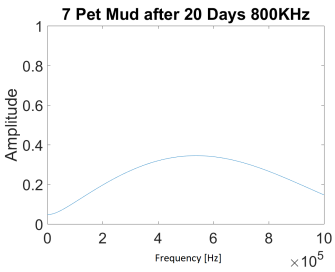

Figure 3.17: Frequency spectrum for P-wave multiple with different centre source frequencies for the Caland mud sample at day 3 and day 21 and for the Petroleum mud sample at day 20.

3.4.2. S-wave frequency analysis

To create an S-wave frequency spectrum, I selected a time coda from the first s arrival until and with the largest amplitude of the S-arrival. An example if this time frame selection can be viewed in Appendix B Figure 3.18 shows that opposed to the more evenly divided frequency spectrum of the P-wave, the frequency spectrum of the S-wave appears to poses more challenges. The reason for this is because the time coda that I have selected for the frequency analysis, could also contain reflected P-wave arrivals and the time coda contains a much larger time frame for the S-wave frequency analysis.

What is also clearly visible is that the frequency spectrum of S-waves shows different trends as time passes, compared to the spectrum of P-waves. After 18 days, it seems that much more of the amplitude is preserved compared to the amplitude after 3 days in the the S-wave frequency spectrum than in the P-wave frequency spectrum. This shows that attenuation increases for P-waves with passing time, where as little changes occurs in the S-wave amplitude with passing time.

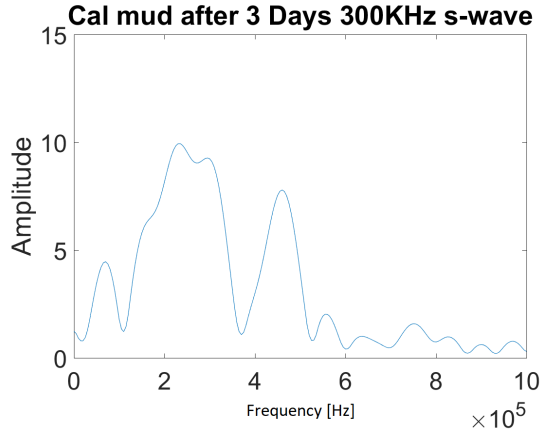

(a) Frequency spectrum with 300 kHz sourc frequency after three days

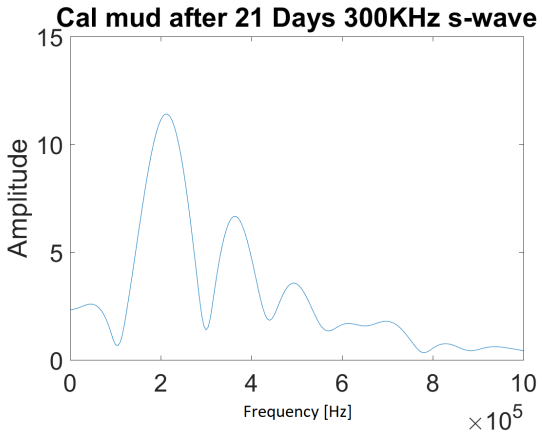

(b) 3600 kHz source frequency spectrum after 21 days

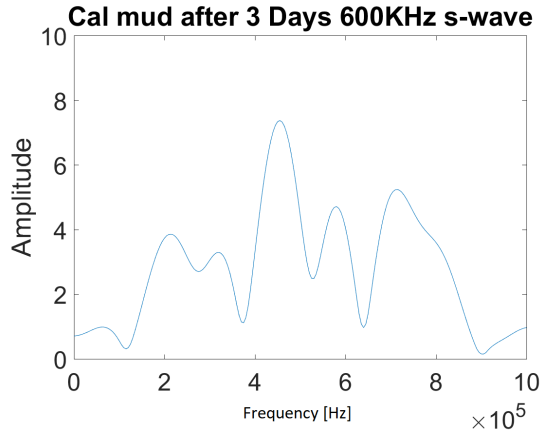

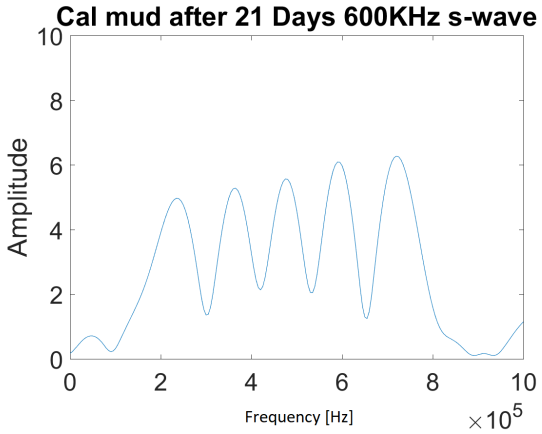

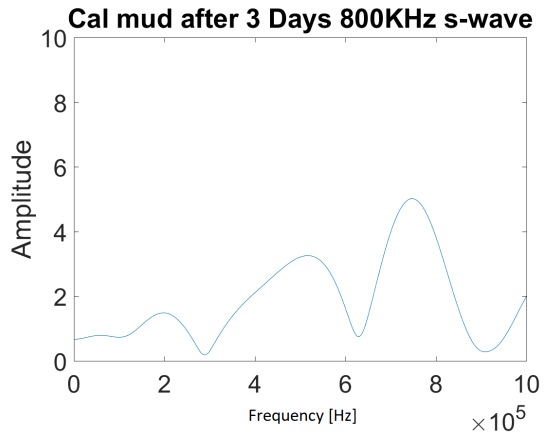

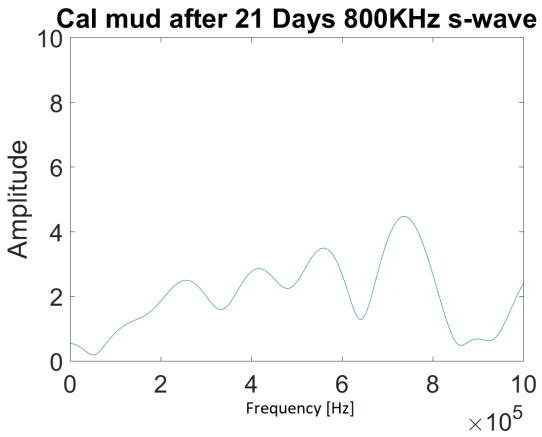

Figure 3.18: Frequency spectrum for S-wave coda with different centre source frequency frequencies

3.5. Forward Model

In order to estimate arrival times of reflections, I have conducted a forward model using a finite-difference scheme in both Seismic Unix, with Fdelmod according to Robbertsson et al. (1994), Bohlen (2002), and Bohlen & Saenger (2004), and a self written finite difference script in Matlab with a PML boundary, according to Liu and Tao (1997). This PML boundary is implement in combination with a large velocity contrast to prevent waves from exiting the cylinder.
This I have done for a circle with a diameter of 9 cm. For the Matlab script, uses the acoustic wave equation. Fdelmod uses the elastic-wave equation, is C based and uses Seismic Unix format to read input data and write output data.
By modeling wave propagation I estimate the arrivals of reflections of 1560 [m/s] for P-waves, and 1050 [m/s] for S-waves. These velocities I derived from my transmission measurements. The reason for creating a forward wave propagation model in both Fdelmod and Matlab is because, Fdelmod did not give satisfying results as will be discussed further on. Also it has a limited time sampling resulting in having to artificially increase the dimensions and decrease the frequencies to compensate for the limited time sampling. A final potential draw back is that Seismic Unix uses a point source by default. It could be that this can be changed to a source with a certain radiation pattern, however due to a time constrain, there was no time to have a further in depth look at Fdelmod and change these settings. In Matlab, I did account for this radation pattern of the source. Also, the frequency and dimensions are not a problem since indexes can be used. The drawback with Matlab is that modelling the elastic-wave equation is quite challenging. Due to a time constrain, therefore the acoustic wave equation is used with an input velocity of both P- and S-wave to estimate traveltimes. Due to the use of the acoustic-wave equation opposed to the elastic wave equation, there will be no converted P- to S-waves, which are be modelled in Seismic Unix.
Figures 3.19, 3.25a and 3.25b show the model space **m** and the forward wave propagation from the Matlab code for P- and S-wave velocities. Figure 3.23 shows the synthetic seismogram with the forward Finite Difference model in Matlab for both P- and S-waves. Figure 3.23 shows that the first break of the S-wave arrival, arrives approximately at the same time as a P-wave reflection. which causes wave interferance for the first S-wave arrival.
Figure 3.22 shows the synthetic seismogram made with Fdelmod.

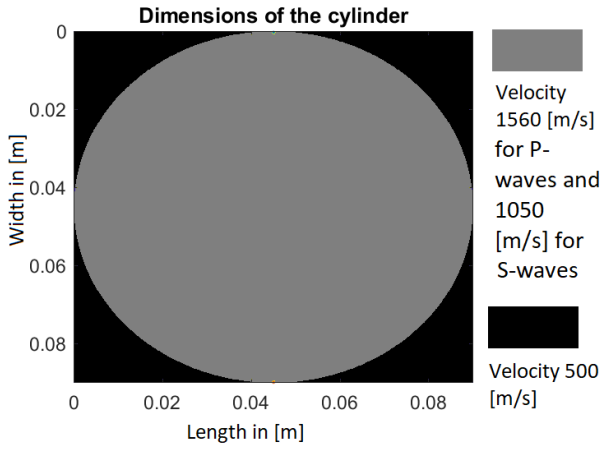

Figure 3.19: Velocity model for the Matlab code representing in grey the cylinder where the velocity is 1560 m/s and in black 500 m/s outside the cylinder. For the S-wave velocity model, the grey area represents 1050 m/s

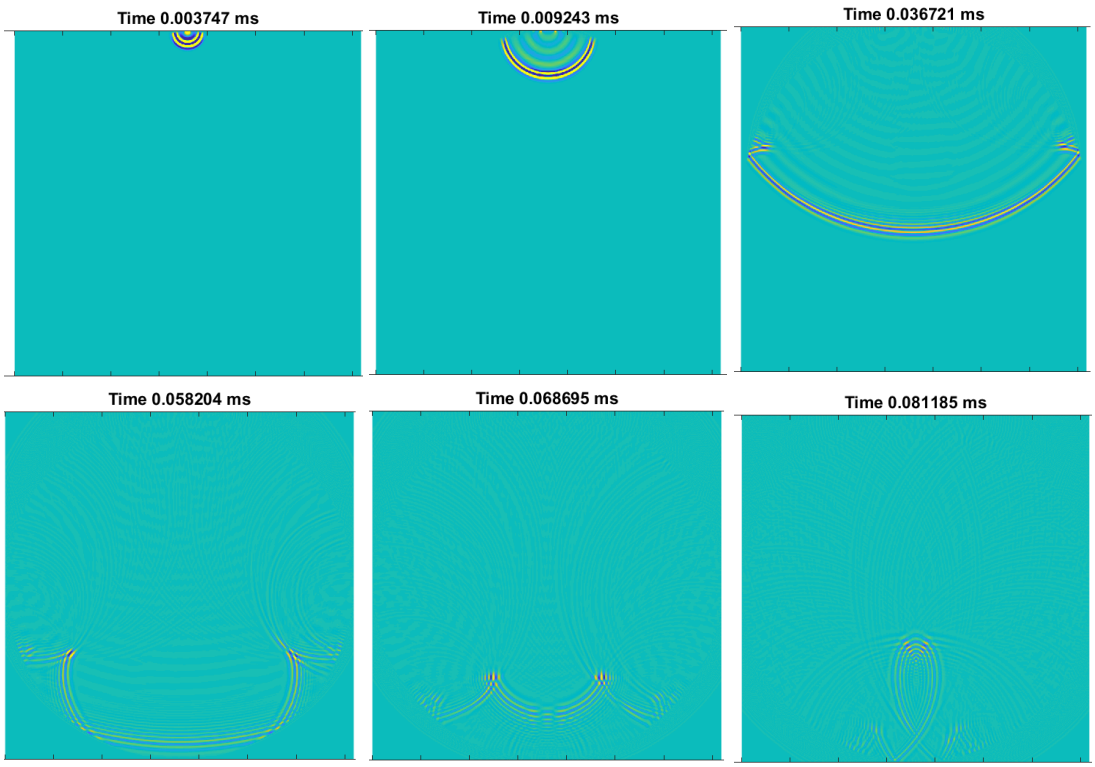

Figure 3.20: Wave propagation with Finite Difference using the Matlab code with the velocity model from Figure 3.19 with the P-wave velocity of 1560 m/s.

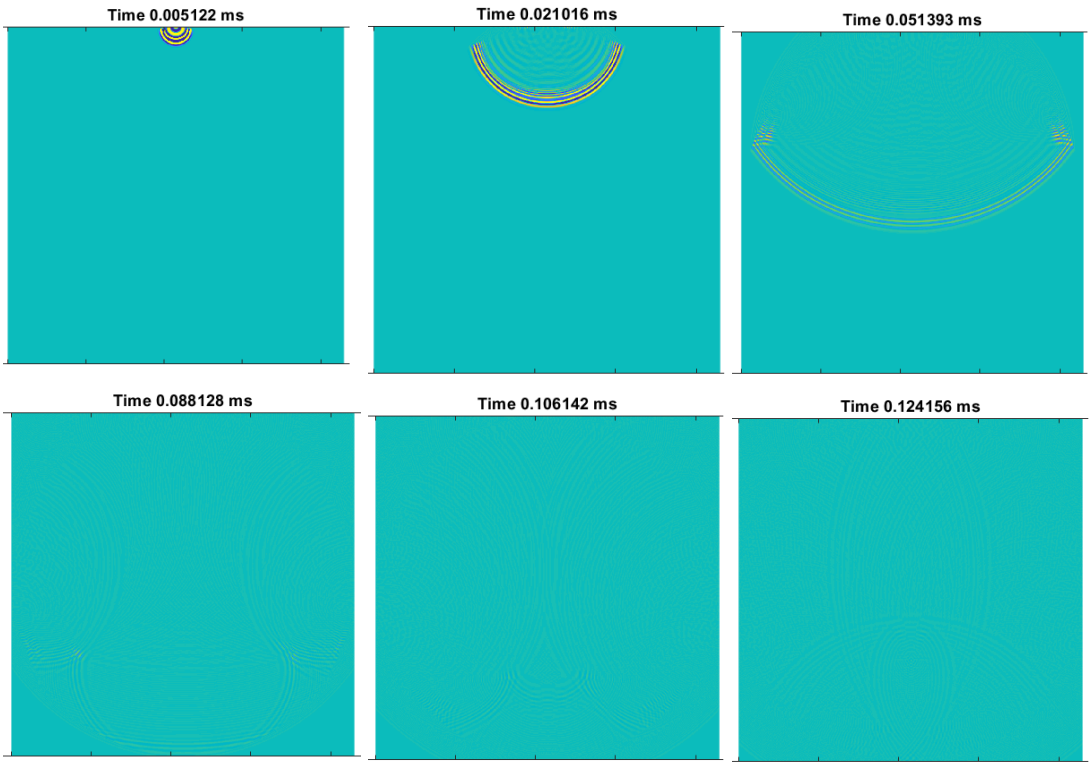

Figure 3.21: Wave propagation with Finite Difference using the Matlab code with the velocity model from Figure 3.19 with the S-wave velocity of 1050 m/s.

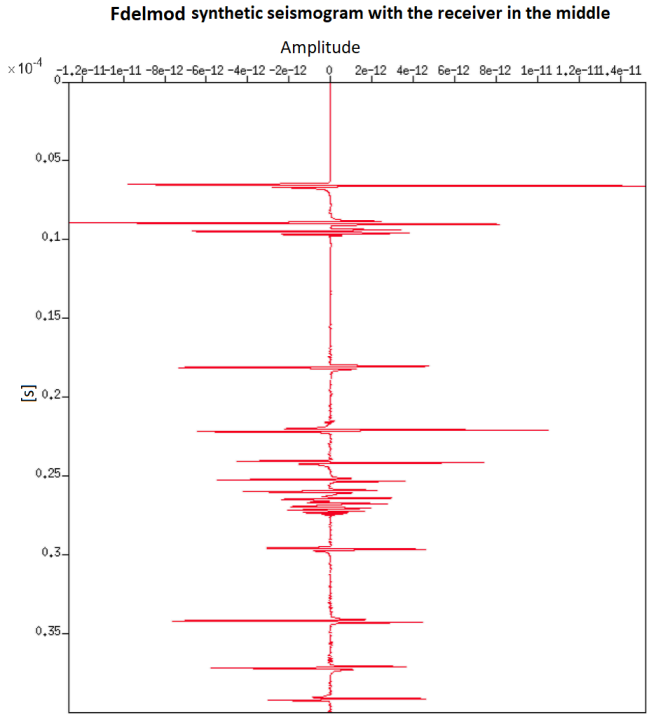

Figure 3.22: Synthetic seismogram made with Fdelmod with the receiver in the middle

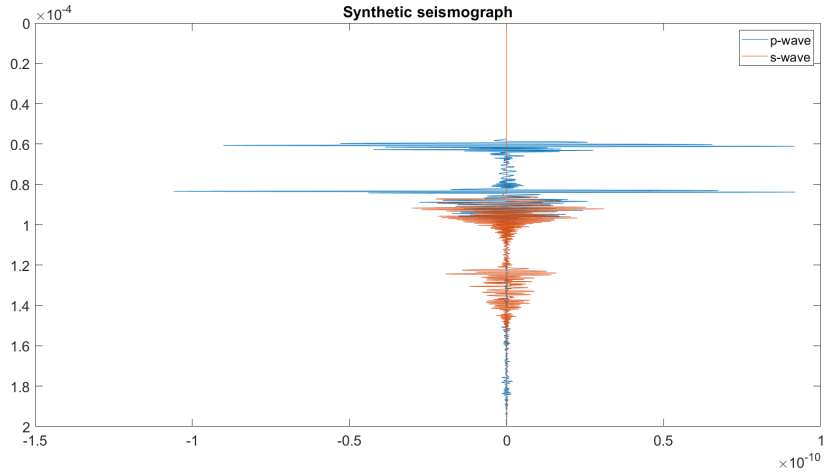

Figure 3.23: Synthetic seismogram made with the Matlab code with P-wave arrivals in blue and S-wave arrivals in orange.

Since the Matlab script is self-written, I compare the trace from Fdelmod, which is trusted and well established, for a quality controll with the Matlab script. This I do for the same configuration as used in Figure 3.22, but now with a receiver shifted 5 mm to allow for easier S-wave detection. It could be easier to detect S-waves since now the receiver is no longer exactly underneath the source. This implies that because of this, the amplitude should be more similar with the real seismogram. By comparing Figure 3.24 with Figures 3.25a, and 3.25b it appears that the P- and S-wave arrivals occur at approximately the same time in the Fdelmod trace compared to the Matlab P-wave seismogram, and the Matlab S-wave seismogram computed with the acoustic wave equation. There is only a difference in the arrival at $01.7 * 10^{-}5$ s in the Fdelmod trace and the arrival at $0.12 * 10^{-}4$ in the S-wave seismogram with the Matlab script. This shows that the Matlab script can be trusted.
Because the arrival times can now be estimated with the Matlab code, it is easier to pick events in both the laboratory data and in the Fdelmod trace. As example, the model shows that a reflected P-wave arrives at almost the same time as the first arrival of the S-wave, around $0.85 * 10^{-}5$. Since the P-wave arrivals can be estimated with the models, it is easier to differentiate between the P-wave arrivals and S-wave arrivals around $0.85 * 10^{-}5$ s. Also, Figure 3.25b shows that around $1.2 * 10^{-}5$, there could be a reflected S-wave. Figure 3.10 shows that there could be an event around that time, but this is very faint however, implying that the S-wave could have attenuated already to much to be detected. This indicates that the attenuation of S-waves is much larger than for P-waves.
Futhermore, by comparing the multiple around $01.7 * 10^{-}5$ in Figure 3.24 Fdelmod with the multiple around $01.7 * 10^{-}5$ in Figure 3.25a, it seems that Fdelmod has a more suitable attenuation factor, since it matches better with the real seismogram in Figure 3.5

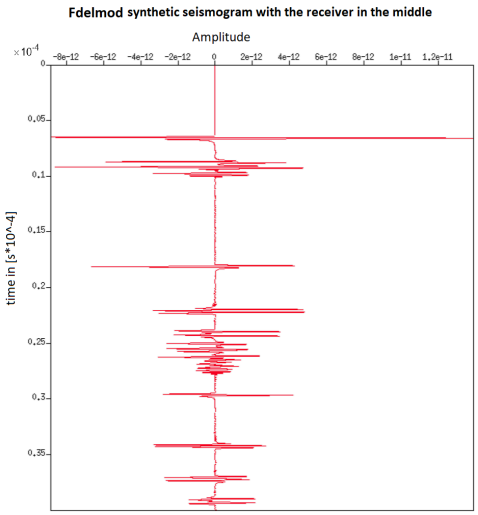

Figure 3.24: Synthetic seismogram made with Fdelmod with the receiver in the shifted 5 mm to the right for better S-wave detection

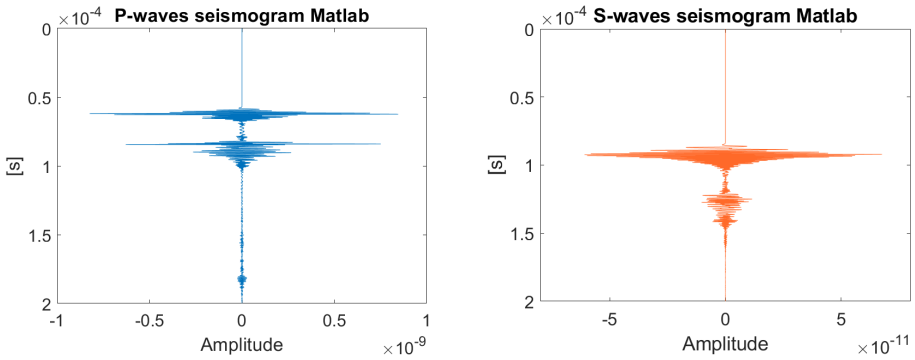

(a) Synthetic seismogram computed with the Matlab code for P-wave arrival approximation.

(b) Synthetic seismogram computed with the Matlab, using the acoustic wave equation with S-wave velocity for S-wave arrivals approximation.

3.6. Reflection measurements

In order to mimic a more applicable setup for the PoR, I also preformed reflection measurements. Figure 3.26 shows the traces from the reflection measurement. This has been done for a mud sample retrieved from the Botlek. The geometry of the transducers is such in to attempt to detect the Scholte wave and converted P- to S-waves. Figure 3.26 shows the results according to the setup of Figure 2.5. The starting offset is 55 mm and the receiver tranducer is moved 2 mm for each trace. It appears that there are mostly linear events visible such as direct waves and refracted waves. Also around $0.6 * 10^{-5}$ - $0.9 * 10^{-5}$ there seems to be a lot of wave interference. This is likely due to the arrival of multiple events.
With the reflection, the starting offset was 75 mm receiver transducer was moved 5 mm for each trace, and the measurements close to the mud, but with a 30 degree angle meaning that the travel path through water increases. Figure 3.27 shows the results of the second reflection measurement. This figure shows a somewhat similar picture as Figure 3.26. Due to the additional water column, the first arrival arrives approximately $0.1 * 10^{-4}$ s later resulting in a shift of all the other arrivals of $0.1 * 10^{-4}$ s. Again there seems to be a lot happening between $0.7 * 10^{-5}$ to $1 * 10^{-5}$ s.

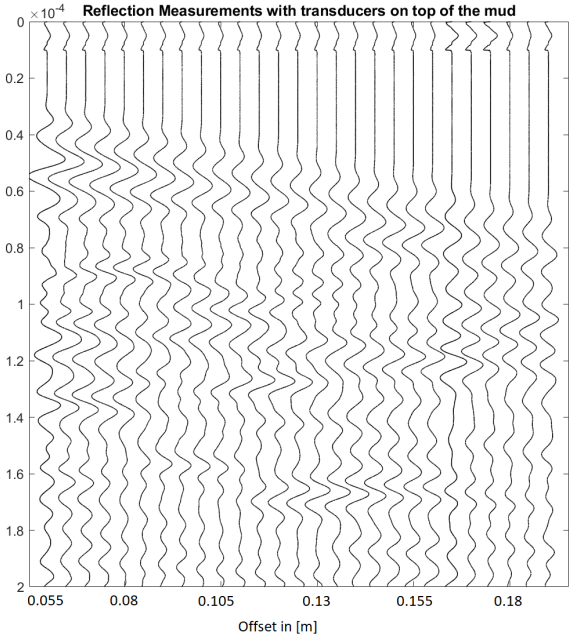

Figure 3.26: Reflection measurements with the setup as described in chapter 2.

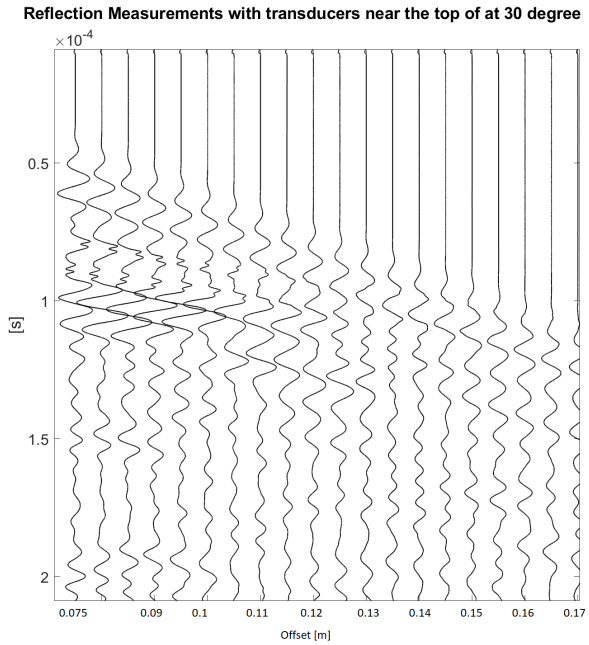

Figure 3.27: Reflection measurements with the transducers slightly higher and at a 30 degree angle.

3.7. Rheological parameters

The static yield point has been derived by conducting a steady stress swipe where a step wise increase in shear stress τ s plotted against the viscosity N/m^2. Then the second incline is picked, which is the elastic/fluid interface as can be seen in Figure 3.28. Here when τ is around 43, the second inclination starts. The result of all the measurements can be seen in table 3.1 and Figure 3.29. Figure 3.29 shows an exponential increase over time, which after some time does not change anymore.

Storage modulus G' and loss modulus G" are frequency depend. The selected frequency to determine G' and G" is 1 Herz. The results can be seen in table 3.1. It appears that there is no clear trend in neither G' or G". This could have been caused by the sampling. The sample for the frequency sweep has been taken from the same bucket after a sample for the steady sweep had been taken, therefore the mud has been disturbed. Since no clear trend can be seen in the development of G' and G", there will be no further analysis of G' and G".

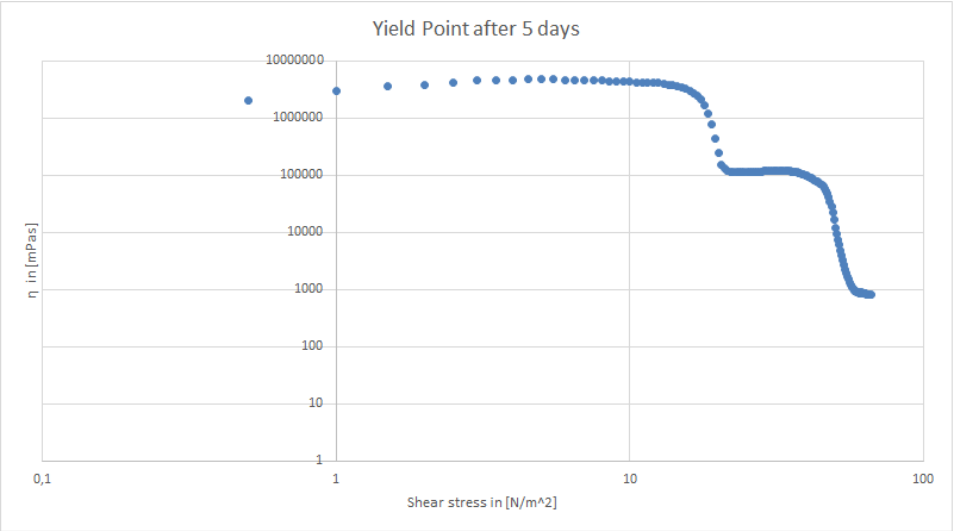

Figure 3.28: Yield Point measurement after the sample has not been disturbed for 5 days

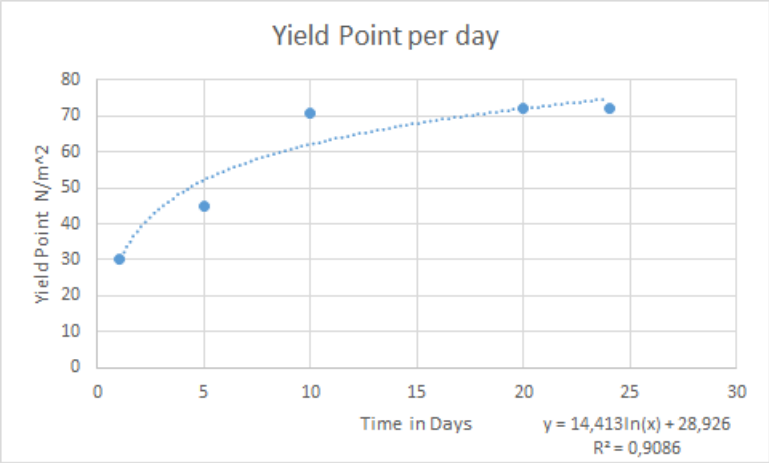

Figure 3.29: Static of fluidic over time for the Caland mud sample for the second declination.

Days	Yield Point $[N/m^2]$	G'	G"
1	30	393	86
5	45	1773	350
10	71	155	26
20	72	7998	1218
24	72	5002	778

Table 3.1: Yield point over time

4

Discussion

In this chapter the findings will be linked to the theory, interpreted and discussed regarding quality. Also recommendations for further research is given and applications for the Port of Rotterdam are suggested.

4.1. Seismic wave development

4.1.1. Seismic Velocities

The most striking result is the high S-wave velocity. Based on previous studies, such as Andres & Stokoe (2000) and Ohta & Goto (1978), I expected S-wave velocities below 600 m/s. The lab experiment showed S-wave velocities over 1000 m/s. Compared to previous literature, this seems at first glance to be too high and because of this, it needs an in depth explanation.

The main difference between these seismic experiments and the conducted experiments from previous literature, is that I used fluid mud, whereas previous studies always measured in soils. Fluid mud contains consists mainly out of water, where as in soils the amount of water is based on pore space. Density of these soils is in general much larger, ranging from approximately 1.4 kg to 2 kg per dm^3, opposed 1.1 kg to 1.3 kg per dm^3 used for the seismic experiments.

It could be that the particle connectivity in mud is almost equal to that of a normal soil, but due to a smaller density, the S-velocities are generally higher. This might seem conflicting with the weak shear strength in fluid mud; however, the S-velocity depends on shear modulus, meaning that shear strength is not the dominate S-wave velocity parameter.

The first reason why I picked my S-wave first break as I did, is due to the different behavior of the S-wave velocity opposed to the P-wave velocity which is visible in Figure 3.11. This figure shows the arrival time of a reflected P-wave and the first break S-wave. It is striking to see that the arrival time of the S-wave decreases whereas the arrival time of that reflected P-wave is more or less stable. The increase in S-wave velocity was expected, since shear strength is building up. Like S-wave velocities, I also expected that P-wave velocities would increase due to compaction, which did not happen. The for why the P-wave velocity development differs from the S-wave velocity development, could be related to some gas production. Gas significantly decrease the compressibility modulus and increases P-wave attenuation. S-waves are hardly affected by gas, since gas does not support S-wave propagation. Therefore S-waves can bypass the gas.

Another interesting difference between the S-wave and P-wave arrivals is that the amplitude of the S-wave seems to be increase opposed to the decreasing amplitude of the P-wave arrivals. The decrease in P-wave arrival amplitude is most notable in Figure 3.5 in the multiple. Potential gas production could result in additional scattering leading to a decrease in amplitude. Also potential increase in compressibility in the fluid mud could be balanced due to increase in gas bubbles in the mud which results in a stable velocity with respect to time. The amount of gas has not been quantified in the mud; however, when I stirred a sample

when it had been staying in a container for a long time, clear gas bubbles rose to the surface. And finally, around $1 * 10^{-4}$ seconds there seems to be an other arrival in Figure 3.10 which could be the converted S- to P-wave wave. This is also visible in Figure 3.22 which could be the calculated S- to P- wave. It appears that this arrival is not clear in the P- transducers, in Figure 3.5. One possible explanation could be that the angle of approximately 45 degrees does not allow for much P- to S-wave conversion, but does allow for S- to P-wave conversion.

4.1.2. Correlation between S-wave velocities and yield-point

It appears that over time the S-wave velocity increases exponentially as can be seen in Figure 4.1. Both S-wave velocity development and yield-stress development show larger changes in the beginning and small changes at the end of the time series. The most interesting feature about the S-wave velocity development is that the development looks very similar to the yield-point development over time. The P-wave velocity development, as seen in Figures 3.7 and 3.8, does not show the same increase and can therefore not be correlated to the increase in yield-point. This shows that S-wave velocities are much more useful to derive the shear strength of fluid mud opposed to conventional P-wave velocities.
There even appears to be a strong linear correlation between S-wave velocities and yield-point with respect to time as can be seen in figure 4.2. However, bare in mind that there are only 5 yield-point measurements and during the sampling of the mud from the rheometer, the mud sample gets disturbed.

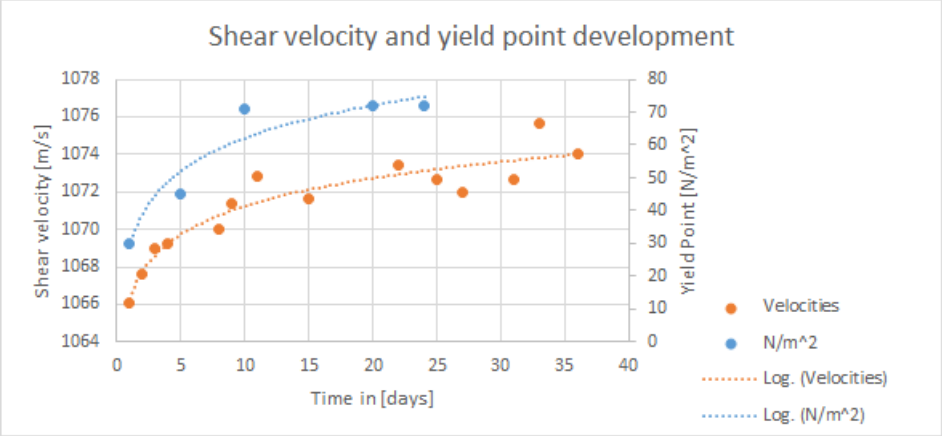

Figure 4.1: S-wave and yield-point development over time

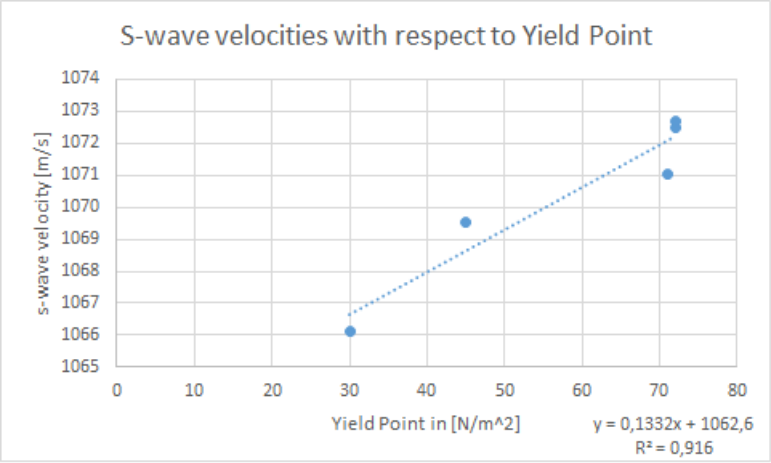

Figure 4.2: S-wave velocities with respect to yield-point. The S-wave velocities are were possible the measured S-wave velocities for the same day as the yield-point has been measured and where else it was interpolated between the nearest points.

4.1.3. Seismic frequencies

The difference between the P-wave and S-wave frequency spectrum indicates that the frequencies in the P-wave spectrum are relatively stable with respect to time, whereas the S-wave frequency spectrum changes much more. This is likely related to the change in rheological properties, such as shear modulus, in the mud over time. Shear modulus increases over time differs. This increase in shear modulus also leads to an increase in S-wave velocity and therefore a changing frequency spectrum. Another reason why the frequency spectrum of the S-wave differs from the P-wave frequency spectrum could be due to the different nature of the waves. Once shear strength builds up in the mud, then this supports S-wave propagation better, resulting in a broader frequency spectrum and an increase in amplitude as well.
What is also notable is that attenuation increases in the P-wave frequency spectrum, opposed to what seems to be a decrease in S-wave spectrum. In the P-wave spectrum, it seems that the relative increase in attenuation is about the same for high frequencies, as well as low frequencies. This could indicate that frequencies higher than 200 kHz are not (much) more prone to gas bubbles.

4.1.4. Difference in forward models

Naturally, due to the different fundamental equations that are used for the forward models for the Matlab simulation and Fdelmod simulation, the models differ. What is however unexpected is that it appears that the forward model with Matlab, using the acoustic wave equation, seems to match the real data better in this specific case, with modeling a cylinder. I expected Fdelmod to give an arrival around $1 * 10^{-5}$, which would be the converted P- to S-wave. There seems to be something arriving around that time in Figure 3.22, but it is a small event. This could mean that there is little P- to S- conversion. At $1.8 * 10^{-5}$ it seems that there is a clear event in Fdelmod. This is likely the multiple. This does not appear as prominent in the real seismogram, nor in the Matlab model. This could mean that there is to little attenuation in Fdelmod for this specific case. With the Matlab model there appears to be to much attenuation. This means that for a more accurate model, more input is needed regarding the attenuation.

4.2. Reflection measurements

The aim of the reflection measurements was to detect either the Scholte wave or the converted P- to S-waves. It is likely that the cap around the transducer prevented the detection of the Scholte wave. Due to a time constraint I was unable to remove the cap. Also converted P- to S-waves were not detected. It could be that the arrival from the converted P- to S-waves interfered with other arrivals. It could be that there is a P- to S-wave around 0.7-1 10^{-4} and that is not detected due to wave interference. It could be that by increasing the size of the mud layer it will be easier to pick the different events since the velocities differ. Also, since the transducers were neither inclined or declined, the amplitude of converted P- to S-waves is likely very small if there is any at all. If the transducers have an angle, then it is likely that much P- to S-wave conversion will occur. The reason why I conducted the measurement without adding an angle to the transducers is because this will add even more distance between the transducer and mud, making recording the Scholte wave even more challenging. If the plastic cap is removed then the added distance by inclining or declining the transducers will be much smaller than with the cap. It could be that due to an expected increase for P- to S-wave conversion, that the amplitude will increase, making the even (more) visible. If this P- to S-wave can be detected, then the S-wave velocity is known and which then can be linked to the yield-point.
Still, there are some clear linear events that can be picked, which are indicated in Figure 4.3.

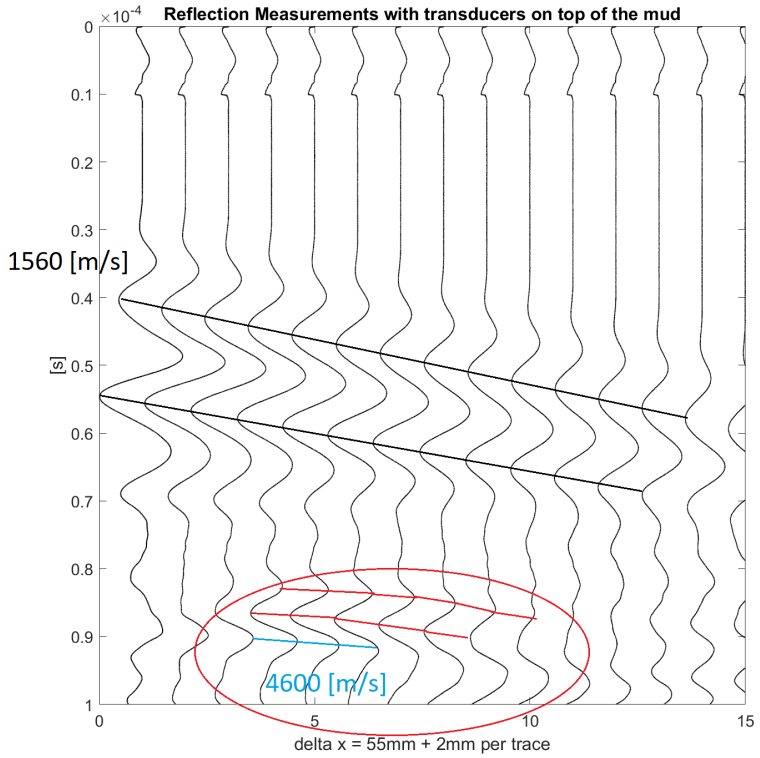

Figure 4.3: Interpretation of the reflection measurements with the flat transducers set-up. Note the line in blue could be a refracted wave, but it could also be a reflection

The first and most obvious arrival is what appear to be the P-wave. Since the offset is fixed and the events linear, the velocity can be calculated by looking at the difference in arrival times with respect of the fixed offset of 2 mm. This velocity is 1560 m/s which indicates it is the direct P-wave traveling through the mud. There also appears to be very fast arrivals, which then will be displayed as very straight lines, such as the one indicated in blue. For this event the same calculation is done and it appears that this event has a velocity 4600 m/s. This velocity is much higher than P-wave velocities in mud and therefore it must be the refracted wave through the glass. It also could be some reflection which with small offsets

would also appear relatively straight (especially at first).
Still there seems to be no linear event that is slower than 1560 m/s meaning that the Scholte wave is not visible in the data. Also it is challenging to pick a hyperbola indicating that the reflections are week, or that they interfere with other arrivals. The mud thickness is known, the arrival of the reflection through the mud can be estimated. This is estimated at around $5.2 * 10^{-5}$ seconds. At the first traces around this time there seem to be many events present, which could mask the reflection arrival. In further traces, it could be that there are no reflections due to signal attenuation.
With the reflection measurements with the transducers a bit higher above the water/mud interface at a 30 degree angle, it seems that the reflections have to be rather steep. Assuming a velocity of the P-waves in the mud of 1560 m/s and 1480 m/s for water I calculated the possible reflection arrival times. Figure 4.4 shows that the estimated arrival times for a reflection appear as a relative straight line, due to the small offsets and the missing near offsets, which should show the apex of the hyperbola. This makes differentiating between the hyperbolas from refractions and other linear events rather challenging.
The reflection in Figure 4.4is; however, estimated and not exact due to the uncertainty caused by the cap around the transducer. It is difficult to determine at which height exactly the receiver senses the P-waves.

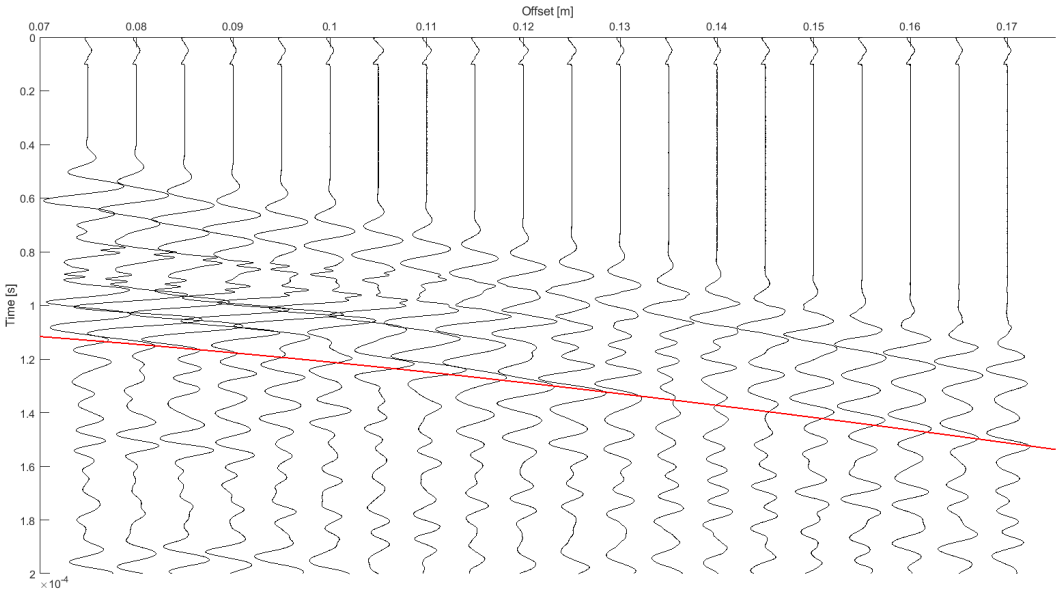

Figure 4.4: In red are the calculated reflection arrival times. This appears to be an almost straight line.

4.3. Application for the Port of Rotterdam

It appears that there is a linear relation between S-wave velocities and yield-point over time. However, because the absolute change in S-wave velocity is approximately 0.8 %, it would be necessary to do a multi-parameter inversion. This can be problematic due to the different rheological properties per channel, or even within the same channel. Luckily, the frequency analysis shows that the difference with respect to time for the same mud is rather small, meaning that the rheological properties might not be very different after all. Also the difference between the two mud samples indicates that the overall difference in frequency spectrum is small as well. Note that, this has only been shown for two mud samples. Nevertheless, it does indicate that the overall difference in mud might be smaller than first assumed. This is beneficial when making a synthetic seismogram, since it will be easier to correlate the synthetic seismogram to seismic data. With the current method, SILAS, also a synthetic seismogram is needed. This seismogram is, however, only dependent on density, meaning that a multi-parameter seismogram could substantially increase the accuracy of the monitoring campaign.
Since elastic-waves will be used and not only acoustic-waves, it is very likely that seasonality will cause problems. During the summer, biological production in the PoR will be at its highest, due to a high organic production in the water channels. This will result in an increase of gas bubbles within the mud. Gas bubbles could seriously distort a seismic image due to an increase in P-wave attenuation, leading to a loss in amplitude. S-waves on the other hand, will hardly be affected by gas, which would mean that imaging with S-waves will not be affected.
During winter occur the most storms in the Netherlands. This could lead to an increase in an-isotrophy and inhomogeneity and might lead to an increase requirement of synthetic seismographs. Ideally, to solve for the inhomogeneity, one could use cross-borehole imaging.

4.3.1. Recommendation

The change in density of the fluid mud, due to consolidation has not been measured, since I was unable to measure the density without disturbing the mud. Information regarding density is likely very valuable to determine shear parameters in fluid mud, together with P- and S-wave velocities. Therefore, I advice for future research to measure density as well, but only if it does not disturb the mud.
The seismic analysis showed that P-wave velocities are likely unsuitable for deriving rheological properties due to gas production. It could be that this would work if there is no gas production within the mud; however, this is unlikely to occur in harbors. Maybe during winter time it would be very limited, but then the measurements would only work during colder seasons. It is likely that further research would be more beneficial if it is focused on S-wave velocities.
For my transmission measurements, I only measured at one height within the cylinder. This was just a few centimeters below the water/mud interface and therefore it is the most 'fluid' part of the fluid mud. It would be beneficial to also mount transducers in the middle or lower part of the mud column to see if the change in velocities differ according to height in the mud section.
Due to the cap on the transducers used for the reflection measurements, I was unable to lower the actual transducer as close to the water/mud interface as needed to record the Scholte wave. It is possible that if the actual transducer is half or a quarter of a wavelength from the water mud/interface, that the Scholte wave can be recorded. For this, the same setup could be used, but then the cap should be either changed, or partly filed off.
Also due the the mission near offsets, differentiating between hyperbolas and linear events challenging. This becomes more difficult since it is impossible to manually shift a transducers exactly 2 mm causing small variations in the offset between the traces. This makes interpretation of the arrivals even more challenging.
In the traces of the Caland mud, there is a clear multiple allowing to derive information on attenuation. This factor could potentially be linked to rheological properties such as viscosity, as described in my theory.

Potentially, more information can be derived from the dispersion relation with respect to mud. This would also require more research.

5

Conclusion

For this research, I measured both P-wave and S-wave velocities in fluid mud. Besides the difference velocity development of P- and S-waves, I also look at the difference in frequency spectrum development for P- and S-waves. The S-wave velocities I correlated to yield-point measurements, measured with a rheometer with the same mud sample. In order to identify different arrivals, I used a forward model in Fdelmod, which is Seismic Unix based, and Matlab, with a self written script.
This research shows that there is a clear correlation between S-wave velocities in m/s and yield-stress in N/m^2 build up over time. This correlation could potentially be used to derive yield-point of fluid mud. Both the S-wave velocities and yield-point measurements show an logarithmic increase with respect to time.
Opposed the the S-wave velocities, the P-wave velocities do not show a clear trend. This might be caused by gas production, which hardly affects S-waves. This shows that only S-wave velocities can be used to monitor shear-stress development over time and derive the yield-point in mud, and that P-wave velocities are of little to no use for such matter.
The high S-wave velocities shows that there is a strong particle connection between the silt particles. This means that attenuation will be smaller allowing for both higher frequencies and larger dimensions to be used when one wants to use S-waves for shear-parameters detection in fluid mud.
Due to the different nature of P- and S-waves, one can distinguish between the two waves with respect to their change in arrival times over time. However, due to the small amplitude, which is caused by limited S-wave propagation support in fluid mud and by a coupling effect of the transducers, it might be challenging, to identify the first breaks. A forward model could be helpful estimate P-wave arrivals and S-wave arrivals, allowing for easier P- or S-wave picking.
It is possible that for P-waves a central frequency of 390 kHz is more beneficial for imaging mud with P-waves, opposed to the commonly used 200 kHz. This central frequency appears in the frequency spectrum for multiple source frequencies, for different mud samples and even for the same mud sample at different times, This shows that this frequency is suitable for at least a very large part of the Port of Rotterdam and that the difference in mud with respect to their P-wave frequency spectrum, is rather small. A drawback of a higher frequency, 390 kHz instead of 200 kHz, is that attenuation will be larger.
Even when the structure of fluid mud is completely destroyed, it does seem that it still can support shear waves. Because of this, the yield-stress will likely change over time according to the Herschel-Bulkey Model.

Bibliography

Aki, K., & Richards, P. (2002). Quantitative seismology. University Science Books .

Allegra, J., & Hawley, S. (1972). Attenuation of sound in suspensions and Emulsions: Theory and Experiments. J. Acoust. Soc AM. 51, 1545-1564.

Andrus, R. D., & Stokoe II, K. H. (2000). Liquefaction resistance of soils from shear-wave velocity. Journal of geotechnical and geoenvironmental engineering, 126(11), 1015-1025.

Barry, C. T., Mills, B., Hah, Z., Mooney, R. A., Ryan, C. K., Rubens, D. J., & Parker, K. J.-1. (2012). Shear wave dispersion measures liver steatosis. Ultrasound in medicine & biology, 38(2), 175-182.

Blackstock. (2001). Fundamentals of physical acoustics.

Bohlen, T. (2002). Parallel 3-d viscoelastic finite difference seismic modelling. Computer and Geosciences, 28:887–899.

Chen, S., Fatemi, M., & Greenleaf, J. F. (2004). Quantifying elasticity and viscosity from measurement of shear wave speed dispersion. The Journal of the Acoustical Society of America, 115(6), 2781-2785.

Dahlen, F., & Tromp, J. (1998). Theoretical global seismology. Princeton University Press.

De Hoop, M. V. (1992). Directional Decomposition of Transient Acoustic Wave Fields,. Delft: Ph.D. thesis, Delft University of Technology.

Donoghue, J. F. (1995). Dispersion Relations and Effective Field. MA 01003 U.S.A.: Department of Physics and Astronomy Amherts.

Drijkoningen, G., el Allouche, N., Thorbecke, J., & Bada, G. (2012). Nongeometrically converted shear waves in marine streamer data. Geophysics, 77(6):45–56.

Fichtner, A. (2012). Full seismic waveform modelling and inversion. Trieste, Italy: The international Union of Geodesy and Geophysics.

Fontein, W., & Van Der Wal, J. (2006). Assessing nautical depth efficiently in terms of rheological characteristics. In Proceedings of International Hydrographic Conference-Hyrdo (Vol. 6).

Hay, A., & Burling, R. (1982). On sound scattering and Attenuation in Suspensions, with Applications. J. Acoust. Soc. AM., 72, 950-959.

Hay, A., & Mercer, D. (1985). On the theory of sound scattering and viscous absorption in aqueous suspensions at medium and short wavelengths. J. Acoust. Soc. AM., 78, 1761-1771.

Hemphill, T., Campos, W., & Pilehvari, A. (1993). Yield-Power Law Model More Accurately Predicts Mud Rheology. Oil & Gas Journal 91c, 45–50.

Huang, X., & Garcia, M. H. (1997). A perturbation solution for Bingham-plastic mudflows. Journal of Hydraulic Engineering, 123(11), 986-994.

Kennett, B. (2001). The Seismic Wavefield Volume I: Introduction and Theoretical Development. Cambridge: Cambridge University Press.

Khataniar, S., Chukwu, A. G., & Xu, H. (1994). Evaluation of rheological models and application to flow regime. Journal of Petroleum Science and Engineering, 155-164.

Kiprop, V. (1. March 2018). The busiest Cargo Ports in Europ. Von World Atlas: https://www.worldatla
busiest-cargo-ports-in-europe.html

Kirichek, A., Chassagne, C., Winterwerp, H., Noordijk, A., Rutgers, R., C. Schot, K., . . . Vellinga, T. (2018). HOW NAVIGABLE ARE FLUID MUD LAYERS. Terra et Aqua, 151.

Lewandowski, R., & Chorążyczewski, B. (2010). Identification of the parameters of the Kelvin–Voigt and the Maxwell fractional models, used to modeling of viscoelastic dampers. Poznan: Poznan University of Technology.

Liu, Q. H., & Tao, J. (1997). The perfectly matched layer for acoustic waves in absorptive media. The Journal of the Acoustical Society of America, 102(4), 2072-2082.

Mason, T. G., & Weitz, D. A. (1995). Optical measurements of frequency-dependent linear viscoelastic moduli of complex fluids. Physical review letters, 74(7), 1250.

McAnally, W. H., Schoellhamer, D., Friedrichs, C., Hamilton, D., Hayter, E., . . . Kirby, R. (2007). Management of fluid mud in estuaries, bays and lakes. ii: Measurement, modelling and management. Journal of Hydraulic Engineering, 133(1).

Oestreicher, H. (1951). Field and impedance of an oscillating sphere in a viscoelastic medium with an application to biophysics. J Acoust Soc AM, 23:704-714.

Ohta, Y., & Goto, N. (1978). Empirical shear wave velocity equations in terms of characteristic soil indexes. Earthquake engineering & structural dynamics, 6(2), 167-187.

Robertsson, J. O. A., Blanch, J. O., and Symes, W. W. (1994). Viscoelastic finite-difference modeling. Geophysics, 59(09):1444–1456.

RWS, a. b. (February 2017). Water en milieu. Van Compendium voor de Leefomgeving: https://www.clo.nl/indicatoren/nl056603-temperatuur-oppervlaktewater [In Dutch]

Saenger, E. H. and Bohlen, T. (2004). Finite-difference modeling of viscoelastic and anisotropic wave propagation using the rotated staggered grid. Geophysics, 69(2):583–591.

Schaafsma, A. (1988). Development of silt measuring methods. Delft: Rijkswaterstaat Dienst Getijdewateren Hydro-Instrumentation Department. [in Dutch]

Schrottke, K., Becker, M., Bartholomä, A., Flemming, B., & Hebbeln, D. (2016). Fluid mud dynamics in the Weser estuary turbidity zone tracked by high-resolution side-scan sonar and parametric sub-bottom profiler. Geo-Marine Letters, 26(3), 185-198.

Wapenaar, C., & Berkhout, A. (1989). Elastic wave field exploration: Redatuming of single- and multi- component seismic data. Delft: Delft University of Technology.

Wapenaar, C (n.d.). Lecture notes of Geophysics Special Subjects AES1550-60 (M.Sc. Applied Geophysics). TU Delft.

A

Pickings

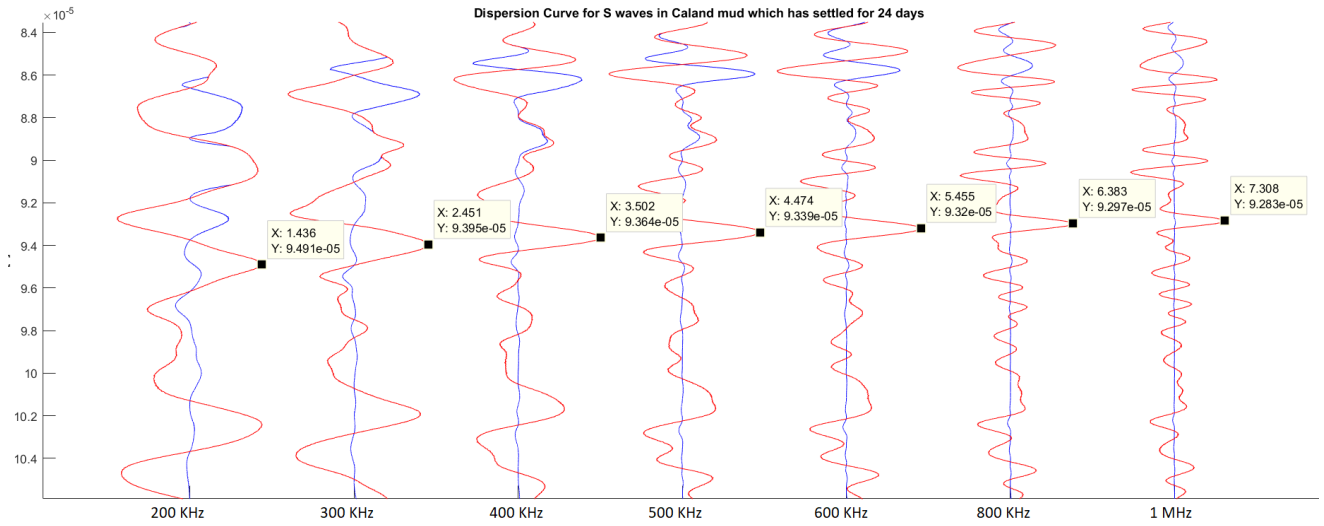

Figure A.1: This specific arrival has been picked since there is no correlation here with the P wave (in blue), meaning there is little to no wave interference and it allows for easy picking.

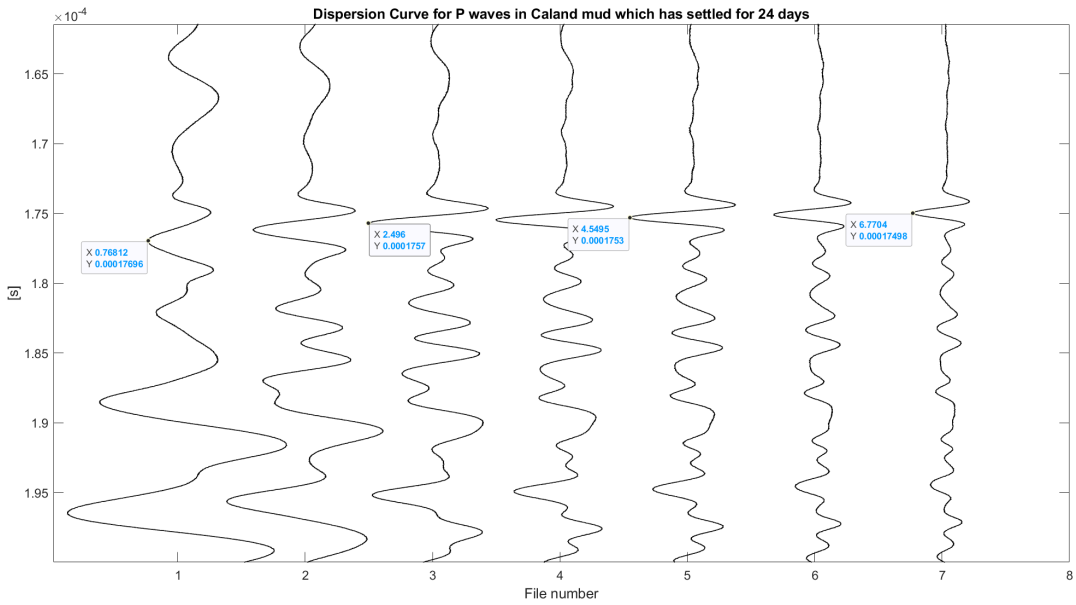

Figure A.2: The multiple has been chosen since it gives a clear amplitude and it is not clipped.

B

Time coda selection

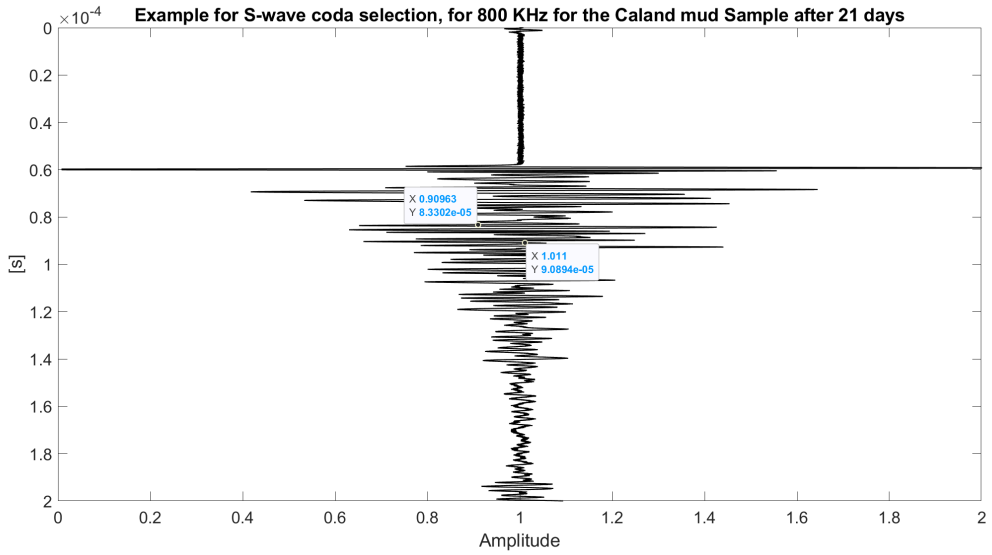

Figure B.1: Time frame selected for the S-wave frequency analysis for a centre source frequency of 800 KHz for the Caland mud sample after 21 days.